

Multi-User Holographic MIMO Surface: Channel Modeling and Spectral Efficiency Analysis

Li Wei, Chongwen Huang, George C. Alexandropoulos, *Senior Member, IEEE*, Wei E. I. Sha, *Senior Member, IEEE*, Zhaoyang Zhang, *Senior Member, IEEE*, Mérouane Debbah, *Fellow, IEEE* and Chau Yuen, *Fellow, IEEE*

Abstract—The multi-user Holographic Multiple-Input and Multiple-Output Surface (MU-HMIMOS) paradigm, which is capable of realizing large continuous apertures with minimal power consumption, has been recently considered as an energy-efficient solution for future wireless networks, offering the increased flexibility in impacting electromagnetic wave propagation according to the desired communication, localization, and sensing objectives. The tractable channel modeling of MU-HMIMOS systems is one of the most critical challenges, mainly due to the coupling effect induced by the excessively large number of closely spaced patch antennas. In this paper, we focus on this challenge for downlink multi-user communications and model the electromagnetic channel in the wavenumber domain using the Fourier plane wave representation. Based on the proposed channel model, we devise the maximum-ratio transmission and Zero-Forcing (ZF) precoding schemes capitalizing on the sampled channel variance that depends on the number and spacing of the patch antennas in MU-HMIMOS, and present their analytical spectral efficiency performance. Moreover, we propose a low computational ZF precoding scheme leveraging Neumann series expansion to replace the matrix inversion, since it is practically impossible to perform direct matrix inversion when the number of patch antennas is extremely large. Our extensive simulation results showcase the impact of the number of patch antennas and their spacing on the spectral efficiency of the considered systems. It is shown that the more patch antennas and larger spacing results in improved performance due to the decreased correlation among the patches. In addition, it is demonstrated that our theoretical performance expressions approximate sufficiently well the simulated spectral efficiency, even for the highly correlated cases, thus verifying the effectiveness and robustness of the presented analytical framework.

Index Terms—Channel modeling, multi-user holographic MIMO surface communications, spectral efficiency, Neumann series expansion, wave propagation control.

L. Wei and C. Yuen are with the Engineering Product Development (EPD) Pillar, Singapore University of Technology and Design, Singapore 487372 (e-mails: wei_li@myemail.sutd.edu.sg, yuenchau@sutd.edu.sg).

C. Huang, Wei E. I. Sha, and Z. Zhang are with the College of Information Science and Electronic Engineering, Zhejiang University, Hangzhou 310007, China, and Zhejiang Provincial Key Lab of Information Processing, Communication and Networking (IPCAN), Hangzhou 310007, China, and the International Joint Innovation Center, Zhejiang University, Haining 314400, China (e-mails: {chongwenhuang, weisha, ning_ming}@zju.edu.cn).

G. C. Alexandropoulos is with the Department of Informatics and Telecommunications, National and Kapodistrian University of Athens, Panepistimiopolis Iliissia, 15784 Athens, Greece (e-mail: alexandg@di.uoa.gr).

M. Debbah is with CentraleSupélec, University Paris-Saclay, 91192 Gif-sur-Yvette, France. M. Debbah is also with the Mathematical and Algorithmic Sciences Lab, Paris Research Center, Huawei Technologies France SASU, 92100 Boulogne-Billancourt, France (emails: merouane.debbah@huawei.com).

I. INTRODUCTION

In recent years, the demand for ubiquitous wireless communications is growing due to the explosive development of mobile devices and multimedia applications [1]. To satisfy the expanding demands, the exploitation of the ultimate limits of communication techniques is concerned, and new technologies to provide higher bandwidth and energy efficiency also attract great interest, e.g., TeraHertz (THz) [2] and millimeter-Wave (mmWave) communications [3], as well as extreme Multiple-Input Multiple-Output (MIMO) catering for massive users and throughput [4], [5]. However, more profound requirements for data rate and massive connections are needed for 6-th Generation (6G) wireless communications. In addition, the exploitation of higher frequencies and larger bandwidths brings many challenges.

The MIMO technology attracts wide research interest for higher capacity transmissions these years. In MIMO systems, a Base Station (BS) equipped with multiple antennas serves single or multiple users by spatial multiplexing [6]–[10]. Such technique has potential in improving Spectral Efficiency (SE) by increasing the number of antennas and users. Thus, the massive MIMO, which adopts very large antenna arrays at the BS and serves multiple users, is expected to achieve better performance [11]. When the number of BS antennas grows large, the power consumption reduces and the spectral efficiency improves [12]. In [13], the authors proposed that the hardware distortion in massive MIMO has negligible impact on SE compare with the that in single antenna user case. [14] proposed a cooperative non-orthogonal multiple access based MIMO system model for 6G to improve the capacity of cell edge user and sum channel capacity. [15] analyzed the asymptotic performance of multi-user MIMO communications with different linear receivers. Although massive MIMO communications provide remarkable methods to combat signal attenuation, it still has some issues such as mobility and hardware scalability.

Fortunately, the development of Reconfigurable Intelligent Surface (RIS) and metasurfaces provides a feasible and engaging research direction towards realizing highly flexible antennas at low cost [16]–[20]. Specifically, an RIS is usually comprised of a large number of hardware-efficient and nearly passive reflecting elements, each of which can alter the phase of the incoming signal without requiring a dedicated power amplifier [21]–[23]. Thus, the deployment of RISs enables the manipulation of electromagnetic (EM) field to achieve an

unprecedented level, and brings benefit in low-power, energy-efficient, high-speed, massive-connectivity, and low-latency wireless communications [24]–[30]. Due to its advantages, the research on RIS-assisted communications have gained increasing research interests [31]–[34]. In [35], a novel passive beamforming and information transfer technologies to enhance primary communication were proposed. Furthermore, Non-Orthogonal Multiple Access (NOMA) in RIS-assisted communications was studied in [36] as a cost-effective solution for boosting spectrum/energy efficiency.

Inspired by the potential of RISs in 6G communications, the Holographic MIMO Surface (HMIMOS) concept aims at going beyond massive MIMO [37], [38]. Specifically, HMIMOS incorporates densely packed sub-wavelength patch antennas to achieve programmable wireless environments [39], which is verified to boost competitiveness in many fields, including NOMA, unmanned aerial vehicles, mmWaves, and multi-antenna systems [40]. [37] proved the flexibility of HMIMOS configuration and the advantages in improving SE through intelligent environment configuration. Authors in [41] investigated the mutual coupling matrix in large RIS-assisted single user communication system, and showed that large RIS could achieve super-directivity. Benefiting from these merits, HMIMOS can be integrated into many fields, including the extension of coverage, wireless power transfer, and indoor positioning [37]. However, the full exploitation of HMIMOS is still a challenge due to many non-trivial issues.

One of the main challenges is multi-user channel modeling due to the spatially continuous aperture realized by holographic patch antennas [5]. The traditional channel models are not applicable for various reasons, e.g., the coupling between antennas, their massive numbers, and the surface-to-surface transmission. Thus, the shift towards infinite antennas and operating frequency beyond the THz requires an effective EM model, since traditional independent Rayleigh fading models based on the assumption of far-field electromagnetic propagation might be not applicable [42], [43]. In this regime, the spatially correlated random field cannot be ignored, and a tractable stochastic tool is required to model the channel. [1] derived the beam pattern and channel estimation schemes for holographic RIS-assisted THz massive MIMO systems, however, the channel is modeled in beam domain sparsely and only considers the line-of-sight path. In [44], a spatially correlated small-scale fading model for single user is proposed employing Fourier plane wave representation to generate samples of the random field computationally. Meanwhile, it is also challenging to efficiently analyze the spatially-continuous EM channel theoretically. [45] investigated the number of channel spatial Degrees of Freedom (DoF) in isotropic scattering environments considering spatially-constrained apertures, and it was proved that the spatial DoF is proportional to the surface area, which is distinct from traditional analysis methods. Furthermore, in order to serve multiple users in multi-user HMIMOS (MU-HMIMOS), even through simple linear precoding scheme, such as Zero-Forcing (ZF), it becomes infeasible and impractical due to large amount of patch antennas. In such context, a low computational precoding scheme is necessary.

Motivated by EM channel modeling for single-user in [44], this paper investigates channel modeling for MU-HMIMOS communication systems, and theoretically analyzes the SE of various linear precoding schemes. Typically, the wireless channel empowered by an HMIMOS with infinite patch antennas is assumed to be on continuous EM space in the optimal setting. To facilitate practical applications, the continuous EM channel is sampled according to a specific placement of the array patch antennas. Thus, the communication is considered as a functional analysis problem depends only on geometric relationships, and the involved channel is constructed as a combination of complete basis function set of transmitter/receiver surfaces. In this manner, the ultimate performance for communications, namely the intrinsic capacity of the sampled space wireless channel, can be studied. Specifically, due to the EM channel being characteristic of complete basis functions, the capacity can be theoretically analyzed using the variances of the sampled transmitter/receiver surfaces. In addition, the MU-HMIMOS involves massive patch antennas, thus even the simple linear precoding (e.g., ZF precoding and Minimum Mean-Square Error (MMSE) precoding) is computationally heavy and costly due to the expensive matrix inversion operation [46]–[50]. To avoid matrix inversion, a low-complexity hardware-efficiency ZF precoding scheme, which is based on the Neumann Series (NS) expansion, is investigated. The main contributions of this paper are summarized as follows:

- We introduce a channel model for MU-HMIMOS communication systems using Fourier plane wave approximation. Specifically, the spatially continuous channel is sampled to contain the main information, where the sampling point is dependent on the spacing and total amount of the surface’s patch antennas.
- We investigate the Maximum Ratio Transmission (MRT) and ZF precoding schemes in MU-HMIMOS communications, and we derive the corresponding theoretical capacity capitalizing on the characteristics of the proposed channel model.
- We introduce a low computational ZF precoding scheme leveraging NS expansion to replace the matrix inversion, as it is practically impossible to implement this operation due to the number of patch antennas is extremely large in MU-HMIMOS systems.
- We prove the validity of our theoretical capacity through simulation results and investigate the impact of spacing among the HMIMOS patch antennas, which gives insights on the surface’s design.

The remainder of this paper is organized as follows. In Section II, the proposed EM channel modeling for MU-HMIMOS communication systems is presented. Section III presents the analytical formulas for the SE with the considered precoding schemes and a low complexity NS based ZF precoding scheme. Our simulation results are given in Section IV, while the concluded remarks of the paper are drawn in Section V.

Notation: Fonts a , \mathbf{a} , and \mathbf{A} represent scalars, vectors, and matrices, respectively. \mathbf{A}^T , \mathbf{A}^H , \mathbf{A}^{-1} , \mathbf{A}^\dagger , and $\|\mathbf{A}\|_F$ denote transpose, Hermitian (conjugate transpose), inverse, pseudo-

inverse, and Frobenius norm of \mathbf{A} , respectively. $\mathbf{A}_{i,j}$ or $[\mathbf{A}]_{i,j}$ represents \mathbf{A} 's (i,j) -th element, while $[\mathbf{A}]_{i,:}$ and $[\mathbf{A}]_{:,j}$ stand for its i -th row and j -th column, respectively. $|\cdot|$ and $(\cdot)^*$ denote the modulus and conjugate, respectively. $\text{tr}(\cdot)$ gives the trace of a matrix, \mathbf{I}_n (with $n \geq 2$) is the $n \times n$ identity matrix, and $\mathbf{1}_n$ is a column vector with all ones. $\delta_{k,i}$ equals to 1 when $k = i$ or 0 when $k \neq i$, and \mathbf{e}_n is the n -th unit coordinate vector with 1 in the n -th basis and 0's in each n' -th basis $\forall n' \neq n$. Finally, notation $\text{diag}(\mathbf{a})$ represents a diagonal matrix with the entries of \mathbf{a} on its main diagonal, $\delta(\cdot)$ is the Dirac delta function, and \odot is the Hadamard product.

II. EM CHANNEL MODELING FOR MU-HMIMOS

In this section, the EM channel adopting approximated Fourier plane-wave series expansion for MU-HMIMOS systems is modeled, and this model works in both EM near-field and far-field assumption, i.e., the wave propagation is formulated in terms of plane-waves irrespective of the distance between the transmitter and the receiver [44].

A. System Model

Consider the downlink communication between a BS and a group of M users that are both equipped with HMIMOS, as shown in Fig. 1. The HMIMOS at BS side is comprised of $N_s = N_V N_H$ unit cells, each made from metamaterials that are capable of adjusting their reflection coefficients, and the patch antennas spacing Δ_s is below half of the wavelength λ . The horizontal and vertical length of HMIMOS is $L_{s,x} = N_H \Delta$ and $L_{s,y} = N_V \Delta_s$. The HMIMOS patch antennas at BS end are indexed row-by-row by $n \in [1, N_s]$, thus the location of the n -th patch antenna with respect to the origin is

$$\mathbf{s}_n = [s_x, s_y, s_z] = [0, i(n)\Delta, j(n)\Delta]^T, \quad (1)$$

where $i(n) = \text{mod}(n-1, N_H)$ and $j(n) = \lfloor (n-1)/N_H \rfloor$ are the horizontal and vertical indices of element n , respectively. Notice that $\text{mod}(\cdot, \cdot)$ denotes the modulus operation and $\lfloor \cdot \rfloor$ is the truncation of argument.

If a plane wave is impinging on the HMIMOS from the azimuth angle φ and elevation angle θ , the response vector becomes

$$\mathbf{a}_s(\boldsymbol{\kappa}, \mathbf{s}) = \left[e^{j\boldsymbol{\kappa}(\varphi, \theta)^T \mathbf{s}_1}, \dots, e^{j\boldsymbol{\kappa}(\varphi, \theta)^T \mathbf{s}_{N_s}} \right]^T, \quad (2)$$

where $\boldsymbol{\kappa}(\varphi, \theta) \in \mathbb{R}^3$ is the transmit wave vector

$$\boldsymbol{\kappa}(\varphi, \theta) = \frac{2\pi}{\lambda} [\cos(\theta) \cos(\varphi), \cos(\theta) \sin(\varphi), \sin(\theta)]^T. \quad (3)$$

Similarly, each user is equipped with N_r patch antennas with spacing Δ_r , and $L_{r,x}$ and $L_{r,y}$ are the horizontal and vertical length, respectively. We assume that there are M users, and the location of m -th user is denoted by $\mathbf{r}_m = [r_{m,x}, r_{m,y}, r_{m,z}]$, $m = 1, \dots, M$. The transmit vector is $\mathbf{a}_s(\boldsymbol{\kappa}, \mathbf{s}) = [a_{s,1}(\boldsymbol{\kappa}, \mathbf{s}), \dots, a_{s,N}(\boldsymbol{\kappa}, \mathbf{s})] \in \mathbb{C}^{1 \times N_s}$, with $a_{s,n}(\boldsymbol{\kappa}, \mathbf{s}) = e^{-j\boldsymbol{\kappa}^T \mathbf{s}_n}$, $n = 1, \dots, N_s$. The receive vector is $\mathbf{a}_r(\mathbf{k}, \mathbf{r}) = [a_{r,1}(\mathbf{k}, \mathbf{r}), \dots, a_{r,M}(\mathbf{k}, \mathbf{r})]^T \in \mathbb{C}^{M \times 1}$, with $a_{r,m}(\mathbf{k}, \mathbf{r}) = e^{j\mathbf{k}^T \mathbf{r}_m}$, $m = 1, \dots, M$.

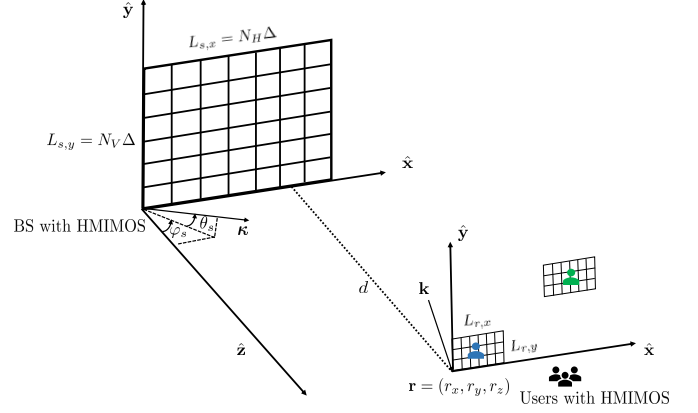


Figure 1: The considered MU-HMIMOS communication system consisting of an N_s patch antennas at BS end and M users with each having N_r patch antennas.

B. Channel Modeling for Individual User

Inspired by Fourier plane-wave representation of electromagnetic channels [44], we model the channel response as a spatially-stationary electromagnetic random field that decouples array geometry and scattering. Specifically, the modeled channel is composed of three parts, i.e., the source response $a_{s,n}(\boldsymbol{\kappa}, \mathbf{s})$, receive response $a_{r,m}(\mathbf{k}, \mathbf{r})$ and angular response $H_a(k_x, k_y, \kappa_x, \kappa_y)$.

Thus, the (m, n) -th entry of channel matrix $\mathbf{H} \in \mathbb{C}^{N_r \times N_s}$ is [44]

$$[\mathbf{H}]_{mn} = \frac{1}{(2\pi)^2} \iiint_{\mathcal{D} \times \mathcal{D}} a_{r,m}(\mathbf{k}, \mathbf{r}) H_a(k_x, k_y, \kappa_x, \kappa_y) a_{s,n}(\boldsymbol{\kappa}, \mathbf{s}) dk_x dk_y d\kappa_x d\kappa_y, \quad (4)$$

where

$$H_a(k_x, k_y, \kappa_x, \kappa_y) = S^{1/2}(k_x, k_y, \kappa_x, \kappa_y) W(k_x, k_y, \kappa_x, \kappa_y) = \frac{\kappa \eta A(k_x, k_y, \kappa_x, \kappa_y) W(k_x, k_y, \kappa_x, \kappa_y)}{2 k_z^{1/2}(k_x, k_y) \kappa_z^{1/2}(\kappa_x, \kappa_y)}, \quad (5)$$

where the spectral factor $A(k_x, k_y, \kappa_x, \kappa_y)$ is an arbitrary real-valued, non-negative function, and $W(k_x, k_y, \kappa_x, \kappa_y)$ is a collection of unit-variance independent and i.i.d. circularly-symmetric and complex-Gaussian random variables. i.e., $W(k_x, k_y, \kappa_x, \kappa_y) \sim \mathcal{CN}(0, 1)$. The spectral density is $S(k_x, k_y, \kappa_x, \kappa_y) = \frac{A^2(k_x, k_y, \kappa_x, \kappa_y)}{k_z(k_x, k_y) \kappa_z(\kappa_x, \kappa_y)}$, and the integration region is $\mathcal{D} = \{(k_x, k_y) \in \mathbb{R}^2 : k_x^2 + k_y^2 \leq \kappa^2\}$, $\kappa = 2\pi/\lambda$.

The former Fourier plane-wave spectral representation can be approximated using the following Fourier plane-wave series expansion. Specifically, the transmit vector and receive vector of one user are rewritten as

$$\begin{aligned} a_s(m_x, m_y, \mathbf{s}) &= e^{-j\left(\frac{2\pi}{L_{s,x}} m_x s_x + \frac{2\pi}{L_{s,y}} m_y s_y + \gamma_s(m_x, m_y) s_z\right)}, \\ a_r(\ell_x, \ell_y, \mathbf{r}) &= e^{j\left(\frac{2\pi}{L_{r,x}} \ell_x r_x + \frac{2\pi}{L_{r,y}} \ell_y r_y + \gamma_r(\ell_x, \ell_y) r_z\right)}, \end{aligned} \quad (6)$$

with

$$\begin{aligned}\gamma_s(m_x, m_y) &= \kappa \sqrt{1 - \left(\frac{\lambda m_x}{L_{s,x}}\right)^2 - \left(\frac{\lambda m_y}{L_{s,y}}\right)^2}, \\ \gamma_r(\ell_x, \ell_y) &= k \sqrt{1 - \left(\frac{\lambda \ell_x}{L_{r,x}}\right)^2 - \left(\frac{\lambda \ell_y}{L_{r,y}}\right)^2}.\end{aligned}\quad (7)$$

In fact, (6) can be regarded as the approximation of the transmit space and receive space, i.e., the basis functions of the two volumes. $H_a(k_x, k_y, \kappa_x, \kappa_y)$ is the coupling matrix between these two spaces, which is only dependent on the scattering environment and array geometry. On the other hand, the more eigenvalues $H_a(k_x, k_y, \kappa_x, \kappa_y)$ has, the more strongly connected channels exist.

The Fourier plane-wave series expansion is non-zero only within the lattice ellipse

$$\begin{aligned}\mathcal{E}_s &= \left\{ (m_x, m_y) \in \mathbb{Z}^2 : (m_x \lambda / L_{s,x})^2 + (m_y \lambda / L_{s,y})^2 \leq 1 \right\}, \\ \mathcal{E}_r &= \left\{ (\ell_x, \ell_y) \in \mathbb{Z}^2 : (\ell_x \lambda / L_{r,x})^2 + (\ell_y \lambda / L_{r,y})^2 \leq 1 \right\},\end{aligned}\quad (8)$$

at the source and receiver, respectively. The cardinalities of the sets \mathcal{E}_s and \mathcal{E}_r are $n_s = |\mathcal{E}_s|$ and $n_r = |\mathcal{E}_r|$, respectively. For $\min(L_{s,x}, L_{s,y}) / \lambda \gg 1$ and $\min(L_{r,x}, L_{r,y}) / \lambda \gg 1$, we have $n_s \approx \lfloor \frac{\pi}{\lambda^2} L_{s,x} L_{s,y} \rfloor$ and $n_r \approx \lfloor \frac{\pi}{\lambda^2} L_{r,x} L_{r,y} \rfloor$. This assumption is similar to the Nyquist sampling theorem for approximating channel as a finite number of basis functions. Thus, to facilitate the MU-HMIMOS communications, we normally have $N_s \geq n_s$ and $N_r \geq n_r$ patch antennas installed at BS and each user, respectively.

Adopting Fourier plane-wave series expansion, we have

$$\begin{aligned}[\mathbf{H}]_{mn} &\approx \sum_{(\ell_x, \ell_y) \in \mathcal{E}_r} \sum_{(m_x, m_y) \in \mathcal{E}_s} H_a(\ell_x, \ell_y, m_x, m_y) \\ &\quad a_{r,m}(\ell_x, \ell_y, \mathbf{r}) a_{s,n}(m_x, m_y, \mathbf{s}),\end{aligned}\quad (9)$$

where the Fourier coefficient is

$$H_a(\ell_x, \ell_y, m_x, m_y) \sim \mathcal{N}_{\mathbb{C}}(0, \sigma^2(\ell_x, \ell_y, m_x, m_y)), \quad (10)$$

with the variance given by

$$\frac{1}{(2\pi)^4} \iiint \iiint_{\mathcal{S}_s \times \mathcal{S}_r} S(k_x, k_y, \kappa_x, \kappa_y) dk_x dk_y d\kappa_x d\kappa_y, \quad (11)$$

where the sets \mathcal{S}_s and \mathcal{S}_r are defined as

$$\begin{aligned}\left\{ \left[\frac{2\pi m_x}{L_{s,x}}, \frac{2\pi(m_x+1)}{L_{s,x}} \right] \times \left[\frac{2\pi m_y}{L_{s,y}}, \frac{2\pi(m_y+1)}{L_{s,y}} \right] \right\}, \\ \left\{ \left[\frac{2\pi \ell_x}{L_{r,x}}, \frac{2\pi(\ell_x+1)}{L_{r,x}} \right] \times \left[\frac{2\pi \ell_y}{L_{r,y}}, \frac{2\pi(\ell_y+1)}{L_{r,y}} \right] \right\}.\end{aligned}\quad (12)$$

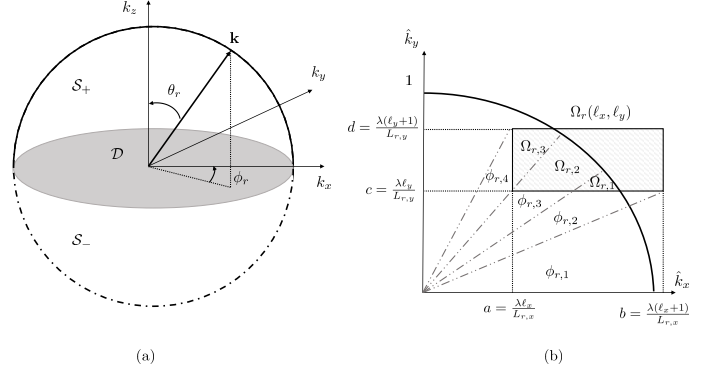


Figure 2: (a) The power spectral density $\mathcal{S}_r(k_x, k_y, \kappa_x, \kappa_y)$ of a spatially-stationary channel; (b) Integration region $\Omega_r(\ell_x, \ell_y)$ of the variances $\sigma^2(\ell_x, \ell_y, m_x, m_y)$.

1) *Computation of Variance $\sigma^2(\ell_x, \ell_y, m_x, m_y)$* : The variance $\sigma^2(\ell_x, \ell_y, m_x, m_y)$ is given as

$$\begin{aligned}\sigma^2(\ell_x, \ell_y, m_x, m_y) &= \frac{1}{(2\pi)^4} \iiint \iiint_{\mathcal{S}_s \times \mathcal{S}_r} S(k_x, k_y, \kappa_x, \kappa_y) dk_x dk_y d\kappa_x d\kappa_y \\ &\propto \iiint \iiint_{\mathcal{S}_s \times \mathcal{S}_r} \mathbb{1}_{\mathcal{D}}(k_x, k_y) \mathbb{1}_{\mathcal{D}}(\kappa_x, \kappa_y) \\ &\quad \frac{A^2(k_x, k_y, \kappa_x, \kappa_y)}{k_z(k_x, k_y) \kappa_z(\kappa_x, \kappa_y)} dk_x dk_y d\kappa_x d\kappa_y \\ &= \iiint \iiint_{\hat{\mathcal{S}}_s \times \hat{\mathcal{S}}_r} \mathbb{1}_{\hat{\mathcal{D}}}(k_x, k_y) \mathbb{1}_{\hat{\mathcal{D}}}(\kappa_x, \kappa_y) \\ &\quad \frac{A^2(\hat{k}_x, \hat{k}_y, \hat{\kappa}_x, \hat{\kappa}_y)}{\hat{k}_z(\hat{k}_x, \hat{k}_y) \hat{\kappa}_z(\hat{\kappa}_x, \hat{\kappa}_y)} d\hat{k}_x d\hat{k}_y d\hat{\kappa}_x d\hat{\kappa}_y,\end{aligned}\quad (13)$$

where $\mathbb{1}_{\mathcal{D}}(\cdot)$ accounts for constants that are embedded into the spectral factor $A^2(k_x, k_y, \kappa_x, \kappa_y)$ to meet the unit average power constraint, and $\hat{\mathcal{D}}$ is a centered disk of radius 1. The normalized wavevector coordinates $(\hat{k}_x, \hat{k}_y, \hat{k}_z) = (k_x, k_y, k_z)/k$. $\mathbb{1}_{\mathcal{D}}(k_x, k_y)$ also implies that $\hat{k}_z \in [0, 1]$, and the normalized coordinates $(\hat{k}_x, \hat{k}_y, \hat{k}_z)$ are the cosine directions of receive response direction \mathbf{k} .

We take the integration in the first wavenumber quadrant as example, thus the spherical coordinates $(\hat{k}_x, \hat{k}_y) = (\sin \theta_r \cos \phi_r, \sin \theta_r \sin \phi_r)$ with elevation angle $\theta_r \in [0, \pi/2]$ and azimuth $\phi_r \in [0, 2\pi]$, which yields $\hat{k}_z = \cos \theta_r \in [0, 1]$, as shown in Fig. 2. It should be noted that we only consider the wave propagating towards $+k_z$ axis, i.e., \mathcal{S}_+ hemisphere, while the $-k_z$ axis wave propagation in \mathcal{S}_- is ignored. In x - y plane, the coordinate $(\hat{k}_x, \hat{k}_y, \hat{k}_z)$ can be represented using the polar coordinates $\hat{k}_r = \sqrt{\hat{k}_x^2 + \hat{k}_y^2} = \sin \theta_r$ and $\hat{k}_\phi = \phi_r$. To transform the polar coordinates into spherical coordinates, the Jacobian of polar coordinates are given as

$$\begin{aligned}\mathbf{J}(\theta_r, \phi_r) &= \begin{bmatrix} \frac{\partial \hat{k}_r}{\partial \theta_r} & \frac{\partial \hat{k}_r}{\partial \phi_r} \\ \frac{\partial \hat{k}_\phi}{\partial \theta_r} & \frac{\partial \hat{k}_\phi}{\partial \phi_r} \end{bmatrix} = \begin{bmatrix} \cos \theta_r & 0 \\ 0 & 1 \end{bmatrix} \\ &= \cos \theta_r \Rightarrow |\mathbf{J}(\theta_r, \phi_r)| = \cos \theta_r.\end{aligned}\quad (14)$$

The above similar procedure can be extended to transmit response $\hat{\kappa}$.

Thus, the (13) can be rewritten as

$$\begin{aligned}
& \sigma^2(\ell_x, \ell_y, m_x, m_y) \\
&= \iiint \int_{\hat{\mathcal{S}}_s(m_x, m_y) \times \hat{\mathcal{S}}_r(\ell_x, \ell_y)} \mathbb{1}_{[0,1]}(\hat{\kappa}_r) \mathbb{1}_{[0,1]}(\hat{\kappa}_r) \\
& \quad \frac{A^2(\hat{\kappa}_r, \hat{\kappa}_\phi, \hat{\kappa}_r, \hat{\kappa}_\phi) \hat{\kappa}_r \hat{\kappa}_r}{\sqrt{1 - \hat{\kappa}_r^2} \sqrt{1 - \hat{\kappa}_r^2}} d\hat{\kappa}_r d\hat{\kappa}_\phi d\hat{\kappa}_r d\hat{\kappa}_\phi \\
&= \iiint \int_{\hat{\mathcal{S}}_s \times \hat{\mathcal{S}}_r} \mathbb{1}_{[0, \pi/2]}(\theta_r) \mathbb{1}_{[0, \pi/2]}(\theta_s) \\
& \quad A^2(\hat{\kappa}_r, \hat{\kappa}_\phi, \hat{\kappa}_r, \hat{\kappa}_\phi) \sin \theta_r \sin \theta_s d\hat{\kappa}_r d\hat{\kappa}_\phi d\hat{\kappa}_r d\hat{\kappa}_\phi \\
&= \iiint \int_{\hat{\mathcal{S}}_s \times \hat{\mathcal{S}}_r} \mathbb{1}_{[0, \pi/2]}(\theta_r) \mathbb{1}_{[0, \pi/2]}(\theta_s) \\
& \quad A^2(\theta_r, \phi_r, \theta_s, \phi_s) d\Omega_r d\Omega_s \\
&= \iiint \int_{\Omega_s \times \Omega_r} A^2(\theta_r, \phi_r, \theta_s, \phi_s) d\Omega_r d\Omega_s,
\end{aligned} \tag{15}$$

where $d\Omega_r = \sin \theta_r d\hat{\kappa}_r d\hat{\kappa}_\phi$ and $d\Omega_s = \sin \theta_s d\hat{\kappa}_s d\hat{\kappa}_\phi$. The integration region is redefined as

$$\begin{aligned}
\Omega_r(\ell_x, \ell_y) &= \hat{\mathcal{S}}_r(\ell_x, \ell_y) \cap \{\theta_r \in [0, \pi/2], \phi_r \in [0, 2\pi]\}, \\
\Omega_s(m_x, m_y) &= \hat{\mathcal{S}}_s(m_x, m_y) \cap \{\theta_s \in [0, \pi/2], \phi_s \in [0, 2\pi]\}.
\end{aligned} \tag{16}$$

As shown in Fig. 2, in the four vertices of $\hat{\mathcal{S}}_r(\ell_x, \ell_y)$ are represented as a, b, c and d , and these four vertices angularly divide the integration region $\Omega_r(\ell_x, \ell_y)$ into three subregions, i.e., $[\phi_{r,1}, \phi_{r,2}]$, $[\phi_{r,2}, \phi_{r,3}]$ and $[\phi_{r,3}, \phi_{r,4}]$ with $\phi_{r,1} < \phi_{r,2} \leq \phi_{r,3} < \phi_{r,4}$.

With the above region splitting, (15) can be rewritten as

$$\begin{aligned}
\sigma^2(\ell_x, \ell_y, m_x, m_y) &= \sum_{i=1}^3 \sum_{j=1}^3 \iiint \int_{\Omega_{s,j}(m_x, m_y) \times \Omega_{r,i}(\ell_x, \ell_y)} \\
& \quad A^2(\theta_r, \phi_r, \theta_s, \phi_s) d\Omega_r d\Omega_s,
\end{aligned} \tag{17}$$

where $\Omega_{r,i}(\ell_x, \ell_y) = \{(\theta_r, \phi_r) : \theta_r \in [\theta_{r,\min}(\phi_r), \theta_{r,\max}(\phi_r)], \phi_r \in [\phi_{r,i}, \phi_{r,i+1}]\}$.

The region splitting in four orthants is given in Fig. 3, and this figure shows the case $L_{r,x} \leq L_{r,y}$. Through the computation of $\sigma^2(\ell_x, \ell_y, m_x, m_y)$, the variance of individual user EM channel response $H_a(\ell_x, \ell_y, m_x, m_y)$ is obtained, thus the channel can be modeled using these variances.

C. Channel Modeling for Multiple Users

This part extends the individual user channel modeling from the previous subsection to the multi-user case, we assume that different users are independently distributed in space, thus, the multi-user involved channel matrix can be decomposed into multiple channel matrices that corresponds to different users. For simplicity, the isotropic scattering environment is considered. To fully characterize EM channel, the HMIMOS patch antennas $N_s \geq \frac{4}{\lambda^2} L_{s,x} L_{s,y} \geq n_s$ at the BS end, and each user is equipped with $N_r \geq \frac{4}{\lambda^2} L_{r,x} L_{r,y} \geq n_r$ patch antennas if $\min(\Delta_s, \Delta_r) \leq \lambda/2$, where Δ_s and Δ_r are patch

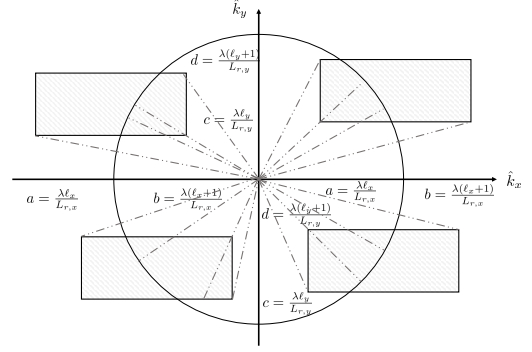


Figure 3: Integration regions $\Omega_r(\ell_x, \ell_y)$ of the variances $\sigma^2(\ell_x, \ell_y, m_x, m_y)$ in four orthants ($L_{r,x} \leq L_{r,y}$).

antennas spacing at BS and user end. The channel of m -th user in matrix form $\mathbf{H}^{(m)} \in \mathbb{C}^{N_r \times N_s}$ is

$$\begin{aligned}
\mathbf{H}^{(m)} &= \sqrt{N_r N_s} \sum_{(\ell_x, \ell_y) \in \mathcal{E}_r} \sum_{(m_x, m_y) \in \mathcal{E}_s} H_a^{(m)}(\ell_x, \ell_y, m_x, m_y) \\
& \quad \mathbf{a}_r(\ell_x, \ell_y, \mathbf{r}^{(m)}) \mathbf{a}_s^H(m_x, m_y, \mathbf{s}),
\end{aligned} \tag{18}$$

where the Fourier coefficient

$$H_a^{(m)}(\ell_x, \ell_y, m_x, m_y) \sim \mathcal{N}_{\mathbb{C}}\left(0, \sigma_{(m)}^2(\ell_x, \ell_y, m_x, m_y)\right), \tag{19}$$

and

$$\begin{aligned}
[a_s(m_x, m_y, \mathbf{s})]_j &= \frac{1}{\sqrt{N_s}} e^{-j\left(\frac{2\pi}{L_{s,x}} m_x s_{xj} + \frac{2\pi}{L_{s,y}} m_y s_{yj} + \gamma_s(m_x, m_y) s_{zj}\right)}, \\
& \quad j = 1, \dots, N_s, \\
[a_r(\ell_x, \ell_y, \mathbf{r}^{(m)})]_i &= \frac{1}{\sqrt{N_r}} e^{j\left(\frac{2\pi}{L_{r,x}} \ell_x r_{xi}^{(m)} + \frac{2\pi}{L_{r,y}} \ell_y r_{yi}^{(m)} + \gamma_r(\ell_x, \ell_y) r_{zi}^{(m)}\right)}, \\
& \quad i = 1, \dots, N_r.
\end{aligned} \tag{20}$$

The N_s entries $[a_s(m_x, m_y, \mathbf{s})]_j$ are collected in $\mathbf{u}_s(m_x, m_y) \in \mathbb{C}^{N_s \times 1}$, and N_r entries $[a_r(\ell_x, \ell_y, \mathbf{r}^{(m)})]_i$ are collected in $\mathbf{u}_r^{(m)}(\ell_x, \ell_y) \in \mathbb{C}^{N_r \times 1}$. Denote $\mathbf{U}_s \in \mathbb{C}^{N_s \times n_s}$ as the matrix collecting the n_s column vectors $\mathbf{u}_s(m_x, m_y)$, and $\mathbf{U}_r^{(m)} \in \mathbb{C}^{N_r \times n_r}$ as the matrix collecting the n_r column vectors $\mathbf{u}_r^{(m)}(\ell_x, \ell_y)$. Specifically, $\mathbf{U}_s \mathbf{U}_s^H = \mathbf{I}_{n_s}$ and $\mathbf{U}_r^{(m)} \mathbf{U}_r^{(m)H} = \mathbf{I}_{n_r}$ since their columns describe discretized transmit and receive plane-wave harmonics.

Based on the above observation, the channel matrix can be approximated by spatial sampling n_s and n_r points at $j = 1, \dots, N_s$ -th patch antenna and the $i = 1, \dots, N_r$ -th received antenna for m -th user. Thus,

$$\mathbf{H}^{(m)} = \mathbf{U}_r^{(m)} \mathbf{H}_a^{(m)} \mathbf{U}_s^H = \mathbf{U}_r^{(m)} \left(\Sigma^{(m)} \odot \mathbf{W} \right) \mathbf{U}_s^H, \tag{21}$$

where $\mathbf{H}_a^{(m)} = \Sigma^{(m)} \odot \mathbf{W} \in \mathbb{C}^{n_r \times n_s}$ collects all $\sqrt{N_r N_s} H_a^{(m)}(\ell_x, \ell_y, m_x, m_y)$, with $\Sigma^{(m)}$ collects all entries $N_r N_s \sigma_{(m)}^2(\ell_x, \ell_y, m_x, m_y)$ and $\mathbf{W} \sim \mathcal{CN}(0, \mathbf{I}_{n_r n_s})$.

Thus, the correlation matrix of one user takes the form

$$\begin{aligned} \mathbf{R}_{\mathbf{H}}^{(m)} &= \mathbb{E} \left\{ \text{vec}(\mathbf{H}^{(m)}) \text{vec}(\mathbf{H}^{(m)})^H \right\} = \left(\mathbf{U}_s^* \otimes \mathbf{U}_r^{(m)} \right) \\ &\mathbb{E} \left\{ \left(\text{vec}(\boldsymbol{\Sigma}^{(m)}) \odot \text{vec}(\mathbf{W}) \right) \left(\text{vec}(\mathbf{W}) \odot \left(\boldsymbol{\Sigma}^{(m)} \right)^H \right) \right\} \\ &\left(\mathbf{U}_s^T \otimes \mathbf{U}_r^{(m)H} \right). \end{aligned} \quad (22)$$

The above derivation focuses on the m -th user channel matrix, here, we consider M users in a general form, we assume that distances between different users are large enough to dependently model channels among users.

Thus, the channel $\mathbf{H} \in \mathbb{C}^{N_r M \times N_s}$ is given by

$$\begin{aligned} \mathbf{H} &= \left[\mathbf{H}^{(1)T}, \dots, \mathbf{H}^{(m)T}, \dots, \mathbf{H}^{(M)T} \right]^T \\ &= \left[\mathbf{U}_s^* \mathbf{H}_a^{(1)T} \mathbf{U}_r^{(1)T}, \dots, \mathbf{U}_s^* \mathbf{H}_a^{(M)T} \mathbf{U}_r^{(M)T} \right]^T \\ &= \mathbf{U}_r \mathbf{H}_a \mathbf{U}_s^H, \end{aligned} \quad (23)$$

where $\mathbf{U}_r \in \mathbb{C}^{M N_r \times M n_r}$ incorporates all received responses for M users, and $\mathbf{H}_a = \left[\mathbf{H}_a^{(1)T}, \dots, \mathbf{H}_a^{(M)T} \right]^T \in \mathbb{C}^{M n_r \times n_s}$ contains all equivalent channels in wavenumber domain for M users.

The correlation matrix is

$$\begin{aligned} \mathbf{R}_{\mathbf{H}} &= \mathbb{E} \{ \text{vec}(\mathbf{H}) \text{vec}(\mathbf{H})^H \} \\ &= \begin{bmatrix} \mathbf{R}_{\mathbf{H}^{(1)}} & 0 & \dots & 0 \\ 0 & \mathbf{R}_{\mathbf{H}^{(2)}} & \dots & 0 \\ 0 & 0 & \ddots & 0 \\ 0 & 0 & \dots & \mathbf{R}_{\mathbf{H}^{(M)}} \end{bmatrix}. \end{aligned} \quad (24)$$

It can be observed from the above equations that the complex spatially correlated channel matrix $\mathbf{H}^{(m)} \in \mathbb{C}^{N_r \times N_s}$ is equivalent to a low-dimensional channel matrix $\mathbf{H}_a^{(m)} \in \mathbb{C}^{n_r \times n_s}$ since $N_s \geq n_s$ and $N_r \geq n_r$.

1) *Isotropic Scattering Environment*: In isotropic scattering environment, $A(k_x, k_y, k_z) = A(k, 0, 0) = A(k)$, we assume that the channel has unit power, thus,

$$\frac{1}{(2\pi)^3} \iiint_{-\infty}^{\infty} A^2(k_x, k_y, k_z) \delta(k_x^2 + k_y^2 + k_z^2 - k^2) dk_x dk_y dk_z = 1. \quad (25)$$

Thus, we have

$$\begin{aligned} A^2(k_x, k_y, k_z) &= \frac{(2\pi)^3}{\iiint_{-\infty}^{\infty} \delta(k_x^2 + k_y^2 + k_z^2 - k^2) dk_x dk_y dk_z} \\ &= \frac{(2\pi)^2}{k} \end{aligned} \quad (26)$$

Under scattering separability, $\boldsymbol{\Sigma}^{(m)} = (\boldsymbol{\sigma}_r^{(m)} \mathbf{1}_{n_s}^T) \odot (\mathbf{1}_{n_r} \boldsymbol{\sigma}_s^T)$, where $\boldsymbol{\sigma}_r^{(m)} \in \mathbb{R}^{n_r \times 1}$ and $\boldsymbol{\sigma}_s \in \mathbb{R}^{n_s \times 1}$ collect $\{\sqrt{N_r} \sigma_r^{(m)}(\ell_x, \ell_y)\}$ and $\{\sqrt{N_s} \sigma_s(m_x, m_y)\}$, respectively. $\sigma_{r,k}^{(m)}$ is the k -th element of $\boldsymbol{\sigma}_r^{(m)}$, and $\sigma_{s,i}$ is the i -th element of $\boldsymbol{\sigma}_s$. The computation of $\sigma_r^2(\ell_x, \ell_y)$ is detailed in Appendix.

III. CAPACITY EVALUATION AND NS BASED ZF PRECODING

In this section, we derive the SE of the downlink MU-HMIMOS communication system adopting linear detectors (MRT and ZF). The perfect knowledge of CSI is obtained at the receiver end, and the phase matrix is assumed to be perfectly configured. Different from the conventional precoding analysis of MIMO system, the MU-HMIMOS system is equipped with a large number of patch antennas at both transmitter and receiver, which requires excessively high computational cost, especially in the matrix inversion operation. In addition, the channel statistics are also different. In traditional MIMO system, each element in channel matrix is normally assumed to have the same unit variance, however, each entry in the constructed EM channel has different variances. Thus, the traditional analysis methods in large MIMO system cannot be directly applied in the considered scenario. Based upon the characteristic of EM, we present a novel capacity evaluation method that requires the less computational cost and a low complexity NS based ZF precoding scheme.

A. Problem Formulation

The HMIMOS at the transmitter is composed of N_s element, and each user is equipped with N_r patch antennas. There are total M users, thus, the downlink MU-HMIMOS wireless communication system model is

$$\mathbf{y} = \sqrt{p_u} \mathbf{H} \boldsymbol{\Phi} \mathbf{V} \mathbf{x} + \mathbf{w} = \sqrt{p_u} \mathbf{U}_r \mathbf{H}_a \mathbf{U}_s^H \boldsymbol{\Phi} \mathbf{V} \mathbf{x} + \mathbf{w}, \quad (27)$$

where $\mathbf{y} \in \mathbb{C}^{N_r M \times 1}$ is the received signal; $\mathbf{H} \in \mathbb{C}^{N_r M \times N_s}$ is the channel matrix; $\boldsymbol{\Phi} = \text{diag}(\boldsymbol{\phi}) \in \mathbb{C}^{N_s \times N_s}$, $\boldsymbol{\phi} = [e^{j\phi_1}, \dots, e^{j\phi_{N_s}}]^T \in \mathbb{C}^{N_s \times 1}$ is the phase vector of HMIMOS part composed of N_s patch antennas. p_u is the transmitted power; $\mathbf{V} \in \mathbb{C}^{N_s \times N_r M}$ is the precoding matrix; $\mathbf{x} \in \mathbb{C}^{N_r M \times 1}$ is the transmitted signal, and $\mathbf{w} \in \mathbb{C}^{N_r M \times 1}$ is additive Gaussian noise that has i.i.d. elements with zero mean and variance σ_w^2 .

Let $\mathbf{y}_a = \mathbf{U}_r^H \mathbf{y} \in \mathbb{C}^{n_r M \times 1}$ the received signal in wavenumber domain, $\tilde{\mathbf{H}}_a = \mathbf{H}_a \mathbf{U}_s^H \boldsymbol{\Phi} \in \mathbb{C}^{n_r M \times N_s}$ is the equivalent channel that incorporates the phase matrix. Thus,

$$\mathbf{y}_a = \sqrt{p_u} \tilde{\mathbf{H}}_a \mathbf{V} \mathbf{x} + \mathbf{w}. \quad (28)$$

The final signal received by m -th user at i -th received sampling point can be given by

$$\begin{aligned} [y_a^{(m)}]_i &= [\tilde{\mathbf{H}}_a^{(m)}]_{i,:} [\mathbf{V}^{(m)}]_{:,i} x_i^{(m)} \\ &+ [\tilde{\mathbf{H}}_a^{(m)}]_{i,:} \sum_{i' \neq i}^{n_r} [\mathbf{V}^{(m)}]_{:,i'} x_{i'}^{(m)} + w_i^{(m)}, \end{aligned} \quad (29)$$

where $\mathbf{x}^{(m)} = [x_1^{(m)}, \dots, x_{N_r}^{(m)}] \in \mathbb{C}^{N_r \times 1}$ is the transmitted signal of m -th user, with $x_i^{(m)}$ the i -th entry. $\mathbf{V}^{(m)} \in \mathbb{C}^{N_s \times N_r}$ is the m -th sub-block in precoding matrix corresponding to the m -th user, and $[\mathbf{V}^{(m)}]_{:,i}$ is the i -th column. $\tilde{\mathbf{H}}_a^{(m)}$ is the m -th sub-block of the channel channel matrix $\tilde{\mathbf{H}}_a$, and $[\tilde{\mathbf{H}}_a^{(m)}]_{i,:}$ is the i -th row. $\mathbf{y}^{(m)} \in \mathbb{C}^{N_r \times 1}$ is the received signal of m -th user, and $[y_a^{(m)}]_i$ is the i -th element. Therefore, the achievable rate

of the m -th user at i -th received response point $i = 1, \dots, n_r$ can be given by

$$\mathcal{R}^{(m),i} = \mathbb{E} \left\{ \log_2 \left(1 + \frac{p_u \left| [\tilde{\mathbf{H}}_a^{(m)}]_{i,:} [\mathbf{V}^{(m)}]_{:,i} \right|^2}{p_u \left| [\tilde{\mathbf{H}}_a^{(m)}]_{i,:} \sum_{i' \neq i}^{n_r} [\mathbf{V}^{(m)}]_{:,i'} \right|^2 + \sigma_w^2} \right) \right\}. \quad (30)$$

B. MRT Precoding

In MRT precoding, $\mathbf{V} = \alpha_{\text{MRT}} \tilde{\mathbf{H}}_a^H$, where α_{MRT} is the normalization coefficient to satisfy the power constraint $\mathbb{E}\{\text{Tr}(\mathbf{V}\mathbf{V}^H)\} = 1$, we have

$$\begin{aligned} \alpha_{\text{MRT}} &= \sqrt{\frac{1}{\mathbb{E}\{\text{Tr}(\tilde{\mathbf{H}}_a \tilde{\mathbf{H}}_a^H)\}}} = \sqrt{\frac{1}{\mathbb{E}\{\text{Tr}(\mathbf{H}_a \mathbf{H}_a^H)\}}} \\ &= \sqrt{\frac{1}{\sum_{i=1}^{n_r} \sum_{j=1}^{n_s} \sigma_{r,i}^2 \sigma_{s,j}^2}}. \end{aligned} \quad (31)$$

This is equivalent to normalize each column of precoding matrix \mathbf{V} , i.e., $\mathbf{V}_{:,i} = \frac{\tilde{\mathbf{g}}_i}{\|\tilde{\mathbf{V}}\|_F}$, where $\tilde{\mathbf{g}}_i$ is the i -th row of equivalent channel $\tilde{\mathbf{H}}_a$, i.e., $\tilde{\mathbf{H}}_a^H = [\tilde{\mathbf{g}}_1, \dots, \tilde{\mathbf{g}}_{n_r}]$, and $\alpha_{\text{MRT}} = \frac{1}{\|\tilde{\mathbf{V}}\|_F}$. Thus,

$$\begin{aligned} \mathcal{R}_{(\text{MRT})}^{(m),i} &= \mathbb{E} \left\{ \log_2 \left(1 + \frac{p_u \alpha_{\text{MRT}}^2 \left| [\tilde{\mathbf{H}}_a^{(m)}]_{i,:} [\tilde{\mathbf{H}}_a^{(m)}]_{:,i} \right|^2}{p_u \alpha_{\text{MRT}}^2 \left| [\tilde{\mathbf{H}}_a^{(m)}]_{i,:} \sum_{i' \neq i}^{n_r} [\tilde{\mathbf{H}}_a^{(m)}]_{:,i'} \right|^2 + \sigma_w^2} \right) \right\} \\ &= \mathbb{E} \left\{ \log_2 \left(1 + \frac{p_u \alpha_{\text{MRT}}^2 \left| [\mathbf{H}_a^{(m)}]_{i,:} [\mathbf{H}_a^{(m)}]_{:,i} \right|^2}{p_u \alpha_{\text{MRT}}^2 \left| [\mathbf{H}_a^{(m)}]_{i,:} \sum_{i' \neq i}^{n_r} [\mathbf{H}_a^{(m)}]_{:,i'} \right|^2 + \sigma_w^2} \right) \right\} \\ &= \mathbb{E} \left\{ \log_2 \left(1 + \frac{p_u \alpha_{\text{MRT}}^2 \left| \mathbf{g}_i^H \mathbf{g}_i \right|^2}{p_u \alpha_{\text{MRT}}^2 \sum_{i' \neq i}^{n_r} \left| \mathbf{g}_i^H \mathbf{g}_{i'} \right|^2 + \sigma_w^2} \right) \right\}, \end{aligned} \quad (32)$$

where \mathbf{g}_i is the i -th column of matrix \mathbf{H}_a^H . The superscript (m) is omitted for the purpose of simplification in the following derivation. To further derive the bound of the MRT precoding system, we adopt Jensen's inequality, specifically,

$$\begin{aligned} \mathcal{R}_{(\text{MRT})}^{(m),i} &\geq \log_2 \left(1 + \left(\mathbb{E} \left\{ \frac{p_u \alpha_{\text{MRT}}^2 \sum_{i' \neq i}^{n_r} \left| \mathbf{g}_i^H \mathbf{g}_{i'} \right|^2 + \sigma_w^2}{p_u \alpha_{\text{MRT}}^2 \left| \mathbf{g}_i^H \mathbf{g}_i \right|^2} \right\} \right)^{-1} \right), \end{aligned} \quad (33)$$

where $\|[\mathbf{H}_a^{(m)}]_{i,:} \mathbf{g}_{i'}\|^2 = n_s \hat{\sigma}_s^2 \sigma_{r,i}^2$, $\|[\mathbf{H}_a^{(m)}]_{i,:} \mathbf{g}_i\|^2 = (n_s^2 + n_s) \hat{\sigma}_s^2 \sigma_{r,i}^2$, and $\|\mathbf{V}\|_F^2 = \sum_{i=1}^{n_r} \sum_{j=1}^{n_s} \sigma_{r,i}^2 \sigma_{s,j}^2 \approx n_s \hat{\sigma}_s^2 \sum_{i=1}^{n_r} \sigma_{r,i}^2$.

Due to

$$\begin{aligned} &\mathbb{E} \left\{ \frac{p_u \alpha_{\text{MRT}}^2 \sum_{i' \neq i}^{n_r} \left| \mathbf{g}_i^H \mathbf{g}_{i'} \right|^2 + \sigma_w^2}{p_u \alpha_{\text{MRT}}^2 \left| \mathbf{g}_i^H \mathbf{g}_i \right|^2} \right\} \\ &= \left(\sum_{i' \neq i}^{n_r} \mathbb{E} \left\{ |\tilde{g}_{i'}|^2 \right\} \right) \mathbb{E} \left\{ \frac{1}{\|\mathbf{g}_i\|^2} \right\} + \mathbb{E} \left\{ \frac{\sigma_w^2}{p_u \alpha_{\text{MRT}}^2 \left| \mathbf{g}_i^H \mathbf{g}_i \right|^2} \right\}, \end{aligned} \quad (34)$$

where $\tilde{g}_{i'} = \frac{\mathbf{g}_i^H \mathbf{g}_{i'}}{\|\mathbf{g}_i\|}$, and \mathbf{g}_i is variable with zero mean and variance $\beta_{i'} = \sigma_{r,i'}^2 \hat{\sigma}_s^2$, where $\hat{\sigma}_s^2 = \frac{1}{n_s} \sum_{j=1}^{n_s} \sigma_{s,j}^2$. We use this

average value to approximate the lower bound in the following derivation.

$$\mathbb{E} \left\{ \frac{1}{\|\mathbf{g}_i\|^2} \right\} = \frac{1}{\sum_{j=1}^{n_s} \sigma_{r,i}^2 \sigma_{s,j}^2} = \frac{1}{(n_s - 1) \hat{\sigma}_s^2 \sigma_{r,i}^2}. \quad (35)$$

$$\mathbb{E} \left\{ \frac{1}{\left| \mathbf{g}_i^H \mathbf{g}_i \right|^2} \right\} = \frac{1}{(n_s - 1)(n_s - 2) \hat{\sigma}_s^4 \sigma_{r,i}^4}. \quad (36)$$

Substituting (35) and (36) into (34), we have

$$\begin{aligned} &\mathbb{E} \left\{ \frac{p_u \alpha_{\text{MRT}}^2 \sum_{i' \neq i}^{n_r} \left| \mathbf{g}_i^H \mathbf{g}_{i'} \right|^2 + \sigma_w^2}{p_u \alpha_{\text{MRT}}^2 \left| \mathbf{g}_i^H \mathbf{g}_i \right|^4} \right\} \\ &= \frac{\hat{\sigma}_s^2 \sum_{i' \neq i}^{n_r} \sigma_{r,i'}^2}{(n_s - 1) \hat{\sigma}_s^2 \sigma_{r,i}^2} + \frac{\sigma_w^2}{p_u \alpha_{\text{MRT}}^2 (n_s - 1)(n_s - 2) \hat{\sigma}_s^4 \sigma_{r,i}^4} \\ &= \frac{p_u (n_s - 2) \hat{\sigma}_s^2 \sigma_{r,i}^2 \sum_{i' \neq i}^{n_r} \sigma_{r,i'}^2 + \sigma_w^2 n_s \sum_{i=1}^{n_r} \sigma_{r,i}^2}{p_u (n_s - 1)(n_s - 2) \hat{\sigma}_s^4 \sigma_{r,i}^4}, \end{aligned} \quad (37)$$

where $\alpha_{\text{MRT}} = \sqrt{\frac{1}{n_s \hat{\sigma}_s^2 \sum_{i=1}^{n_r} \sigma_{r,i}^2}}$. Thus, the theoretical capacity bound is given by

$$\begin{aligned} \tilde{\mathcal{R}}_{(\text{MRT})}^{(m),i} &\geq \log_2 \left(1 + \frac{p_u (n_s - 1)(n_s - 2) \hat{\sigma}_s^2 \sigma_{r,i}^4}{p_u (n_s - 2) \hat{\sigma}_s^2 \sigma_{r,i}^2 \sum_{i' \neq i}^{n_r} \sigma_{r,i'}^2 + \sigma_w^2 n_s \sum_{i=1}^{n_r} \sigma_{r,i}^2} \right) \\ &\stackrel{n_s \gg 2}{\approx} \log_2 \left(1 + \frac{p_u n_s \hat{\sigma}_s^2 \sigma_{r,i}^4}{p_u \hat{\sigma}_s^2 \sigma_{r,i}^2 \sum_{i' \neq i}^{n_r} \sigma_{r,i'}^2 + \sigma_w^2 \sum_{i=1}^{n_r} \sigma_{r,i}^2} \right). \end{aligned} \quad (38)$$

C. ZF Precoding

This precoding scheme intends at eliminating interference among different users by setting the precoding matrix as $\mathbf{V} = \alpha_{\text{ZF}} \tilde{\mathbf{H}}_a^H \left(\tilde{\mathbf{H}}_a \tilde{\mathbf{H}}_a^H \right)^{-1}$, where α_{ZF} is the normalization factor to obey the constraint $\mathbb{E}\{\text{Tr}(\mathbf{V}\mathbf{V}^H)\} = 1$. In this case, it holds $\alpha_{\text{ZF}} \tilde{\mathbf{H}}_a^{(m)} \mathbf{V}^{(m)} = \mathbf{I}_{n_r}$. Specifically, we adopt the vector normalization method in [51], i.e., $\tilde{\mathbf{H}}_a^H \left(\tilde{\mathbf{H}}_a \tilde{\mathbf{H}}_a^H \right)^{-1} = [\mathbf{f}_1, \dots, \mathbf{f}_{n_r}]$, $\mathbf{V}_{:,i} = \frac{\mathbf{f}_i}{\sqrt{n_r} \|\mathbf{f}_i\|}$. Thus, the achievable rate is given by

$$\begin{aligned} \mathcal{R}_{(\text{ZF})}^{(m),i} &= \mathbb{E} \left\{ \log_2 \left(1 + \frac{p_u \left| [\tilde{\mathbf{H}}_a^{(m)}]_{i,:} [\mathbf{V}^{(m)}]_{:,i} \right|^2}{p_u \left| [\tilde{\mathbf{H}}_a^{(m)}]_{i,:} \sum_{i' \neq i}^{n_r} [\tilde{\mathbf{H}}_a^{(m)}]_{:,i'} \right|^2 + \sigma_w^2} \right) \right\} \\ &= \mathbb{E} \left\{ \log_2 \left(1 + \frac{p_u \left| [\mathbf{H}_a^{(m)}]_{i,:} [\mathbf{H}_a^{(m)}]_{:,i} \right|^{-1}}{p_u \alpha_{\text{ZF}}^2 \left| [\mathbf{H}_a^{(m)}]_{i,:} \sum_{i' \neq i}^{n_r} [\mathbf{H}_a^{(m)}]_{:,i'} \right|^{-1} + \sigma_w^2} \right) \right\} \\ &= \mathbb{E} \left\{ \log_2 \left(1 + \frac{p_u \left| [\mathbf{H}_a^{(m)}]_{i,:} \frac{\mathbf{f}_i}{\sqrt{n_r} \|\mathbf{f}_i\|} \right|^2}{p_u \left| [\mathbf{H}_a^{(m)}]_{i,:} \sum_{i' \neq i}^{n_r} \frac{\mathbf{f}_{i'}}{\sqrt{n_r} \|\mathbf{f}_{i'}\|} \right|^2 + \sigma_w^2} \right) \right\} \\ &= \mathbb{E} \left\{ \log_2 \left(1 + \frac{p_u}{n_r \sigma_w^2 \|\mathbf{f}_i\|^2} \right) \right\}. \end{aligned} \quad (39)$$

We adopt the mathematical method in [52] to analyze the theoretical capacity. Due to $\mathbf{f}_i = \tilde{\mathbf{H}}_a^H \left(\tilde{\mathbf{H}}_a \tilde{\mathbf{H}}_a^H \right)^{-1} \mathbf{e}_i$, where \mathbf{e}_i is a column vector that is 1 at i -th entry and 0 otherwise, the term $\frac{1}{\|\mathbf{f}_i\|^2}$ can be given as

$$\begin{aligned}\beta_i &= \frac{1}{\|\mathbf{f}_i\|^2} = \frac{1}{\|\tilde{\mathbf{H}}_a^H \left(\tilde{\mathbf{H}}_a \tilde{\mathbf{H}}_a^H \right)^{-1} \mathbf{e}_i\|^2} \\ &= \frac{1}{\mathbf{e}_i^T (\mathbf{H}_a \mathbf{H}_a^H)^{-1} \mathbf{e}_i} = \frac{\det[\mathbf{H}_a \mathbf{H}_a^H]}{\det[\mathbf{H}_a^{(i)-} [\mathbf{H}_a^{(i)-}]^H]},\end{aligned}\quad (40)$$

where $\mathbf{H}_a^{(i)-}$ is the matrix of \mathbf{H}_a deleting i -th row, and \det denotes the determinant of a matrix. We have

$$\det[\mathbf{H}_a \mathbf{H}_a^H] = \sum_{i=1}^{n_r} (-1)^{i-1} \mathbf{g}_1^H \mathbf{g}_i \det[\mathbf{H}_a^{(1)-} [\mathbf{H}_a^{(i)-}]^H]. \quad (41)$$

Thus,

$$\begin{aligned}\beta_1 &= \frac{1}{\|\mathbf{f}_1\|^2} \\ &= \mathbf{g}_1^H \mathbf{g}_1 - \frac{\sum_{i=2}^{n_r} (-1)^i \mathbf{g}_1^H \mathbf{g}_i \det[\mathbf{H}_a^{(1)-} [\mathbf{H}_a^{(i)-}]^H]}{\det[\mathbf{H}_a^{(1)-} [\mathbf{H}_a^{(1)-}]^H]} \\ &= \mathbf{g}_1^H \mathbf{g}_1 - \sum_{i=2}^{n_r} (-1)^i \mathbf{g}_1^H \mathbf{g}_i \frac{\sum_{k=2}^{n_r} (-1)^{k-1} \mathbf{g}_k^H \mathbf{g}_1 \det[\mathbf{M}_k]}{\sum_{j=2}^{n_r} (-1)^{i+j-1} \mathbf{g}_j^H \mathbf{g}_i \det[\mathbf{M}_j]} \\ &= \mathbf{g}_1^H \mathbf{g}_1 - \sum_{i=2}^{n_r} \frac{\sum_{k=2}^{n_r} (-1)^{k-1} \mathbf{g}_k^H \mathbf{g}_1 \mathbf{g}_1^H \mathbf{g}_i \det[\mathbf{M}_k]}{\sum_{j=2}^{n_r} (-1)^{j-1} \mathbf{g}_j^H \mathbf{g}_i \det[\mathbf{M}_j]},\end{aligned}\quad (42)$$

where \mathbf{M}_k is the sub-block matrix of $\mathbf{H}_a^{(1)-} [\mathbf{H}_a^{(1)-}]^H$ with removal of the k -th row and the i -th column. Using the fact that each element in \mathbf{H}_a is independent, and $\mathbb{E}\{[\mathbf{H}_a]_{i,j}^2\} = \sigma_{r,i}^2 \sigma_{s,j}^2$ under separable scattering environment, we have $\mathbb{E}\{\mathbf{g}_1 \mathbf{g}_1^H\} = \text{diag}[\sigma_{r,1}^2 \sigma_{s,1}^2, \dots, \sigma_{r,1}^2 \sigma_{s,n_s}^2]$. Thus,

$$\begin{aligned}\mathbb{E} \left\{ \frac{\sum_{k=2}^{n_r} (-1)^{k-1} \mathbf{g}_k^H \mathbf{g}_1 \mathbf{g}_1^H \mathbf{g}_i \det[\mathbf{M}_k]}{\sum_{j=2}^{n_r} (-1)^{j-1} \mathbf{g}_j^H \mathbf{g}_i \det[\mathbf{M}_j]} \right\} \\ = \mathbb{E} \left\{ \frac{\sum_{k=2}^{n_r} (-1)^{k-1} \mathbf{g}_k^H \mathbb{E}\{\mathbf{g}_1 \mathbf{g}_1^H\} \mathbf{g}_i \det[\mathbf{M}_k]}{\sum_{j=2}^{n_r} (-1)^{j-1} \mathbf{g}_j^H \mathbf{g}_i \det[\mathbf{M}_j]} \right\} \\ \stackrel{(a)}{=} \sigma_{r,1}^2 \hat{\sigma}_s^2,\end{aligned}\quad (43)$$

where (a) simplifies the derivation using average variances, i.e., $\mathbb{E}\{\mathbf{g}_1 \mathbf{g}_1^H\} = \sigma_{r,1}^2 \hat{\sigma}_s^2 \mathbf{I}_{n_s}$. As a result,

$$\begin{aligned}\mathbb{E}\{\beta_1\} &= \mathbb{E}\left\{\frac{1}{\|\mathbf{f}_1\|^2}\right\} = \mathbb{E}\{\mathbf{g}_1^H \mathbf{g}_1\} \\ &\quad - \mathbb{E}\left\{\sum_{i=2}^{n_r} \frac{\sum_{k=2}^{n_r} (-1)^{k-1} \mathbf{g}_k^H \mathbf{g}_1 \mathbf{g}_1^H \mathbf{g}_i \det[\mathbf{M}_k]}{\sum_{j=2}^{n_r} (-1)^{j-1} \mathbf{g}_j^H \mathbf{g}_i \det[\mathbf{M}_j]}\right\} \\ &\approx \sigma_{r,1}^2 \sum_{j=1}^{n_s} \sigma_{s,j}^2 - (n_r - 1) \sigma_{r,1}^2 \hat{\sigma}_s^2 \\ &= (n_s - n_r + 1) \sigma_{r,1}^2 \hat{\sigma}_s^2.\end{aligned}\quad (44)$$

Based upon the above observation, we can derive the theoretical capacity as

$$\begin{aligned}\tilde{\mathcal{R}}_{(\text{ZF})}^{(m),i} &= \mathbb{E}\left\{\log_2\left(1 + \frac{p_u}{n_r \sigma_w^2 \|\mathbf{f}_i\|^2}\right)\right\} \\ &\approx \log_2\left(1 + \frac{p_u}{n_r \sigma_w^2} (n_s - n_r + 1) \sigma_{r,i}^2 \hat{\sigma}_s^2\right).\end{aligned}\quad (45)$$

D. NS based ZF Precoding

The ZF precoding scheme involves the inverse operation of the $n_r \times n_r$ matrix, a traditional approach is to compute the exact inverse of the matrix $\mathbf{Z} = \mathbf{H}_a \mathbf{H}_a^H$ in

$$\mathbf{V} = \alpha_{\text{ZF}} \mathbf{H}_a^{-1} = \mathbf{H}_a^H (\mathbf{H}_a \mathbf{H}_a^H)^{-1} = \mathbf{H}_a^H \mathbf{Z}^{-1}. \quad (46)$$

This computation would be excessively high as n_r grows large, and even the simple linear ZF precoding is impractical considering extremely large number of patch antennas in MU-HMIMOS communications. Thus, we consider NS expansion to replace the matrix inversion. Specifically, in separable scattering environment,

$$\begin{aligned}\mathbf{Z}^{-1} &= (\mathbf{H}_a \mathbf{H}_a^H)^{-1} \\ &= (\text{diag}(\boldsymbol{\sigma}_r) \mathbf{W} \text{diag}(\boldsymbol{\sigma}_s^2) \mathbf{W}^H \text{diag}(\boldsymbol{\sigma}_r))^{-1} \\ &= \text{diag}(\boldsymbol{\sigma}_r)^{-1} \tilde{\mathbf{W}}^{-1} \text{diag}(\boldsymbol{\sigma}_r)^{-1},\end{aligned}\quad (47)$$

where $\tilde{\mathbf{W}} = \mathbf{W} \text{diag}(\boldsymbol{\sigma}_s^2) \mathbf{W}^H$. $\text{diag}(\boldsymbol{\sigma}_s)$ and $\text{diag}(\boldsymbol{\sigma}_r)$ are diagonal matrix that are easily to compute the matrix inversion, thus the computational cost mainly lies in the computation of $\tilde{\mathbf{W}}^{-1}$. However, the Gram matrix $\tilde{\mathbf{W}}$ is not a strongly diagonally dominant or even not dominant at all in some highly correlated cases, thus, the Neumann method cannot be applied in the computation of $\tilde{\mathbf{W}}^{-1}$ directly, which may result in the slow convergence or even divergence. Fortunately, in the special case of single ended correlation, (i.e., transmit correlation, or receive correlation, but not both are considered), the Neumann method can work well as follows.

In Neumann method, the Gram matrix $\tilde{\mathbf{W}}$ is decomposed into its main diagonal matrix \mathbf{D} and off-diagonal matrix \mathbf{E} [53], i.e., $\tilde{\mathbf{W}} = \mathbf{D} + \mathbf{E}$. The inverse of $\tilde{\mathbf{W}}$ is given by

$$\tilde{\mathbf{W}}^{-1} = \sum_{i=0}^{\infty} (-\mathbf{D}^{-1} \mathbf{E})^i \mathbf{D}^{-1}. \quad (48)$$

Increasing the iteration number i would bring a higher precision of the matrix inversion at a higher computational cost, in this paper, the i is set to be 3 for efficient computation at the low computational cost.

IV. PERFORMANCE EVALUATION

In this section, we present computer simulation results of the downlink SE in the considered MU-HMIMOS system as well as the theoretical capacity. The single-sided correlation [54] and three users are considered. All capacity curves were obtained after averaging over 800 independent Monte Carlo channel realizations.

Fig. 4 illustrates the eigenvalues of channel correlation matrix \mathbf{R}_H in decreasing order in a setup with $N_s = 900$, $N_r = 576$, $\Delta_s = \lambda/3$ for different spacing in received patch antennas. From the figure, eigenvalues are large but non-identical initially, and then the eigenvalues quickly approach zero. This means the strengths of the coupling coefficients are not all equal even in isotropic propagation, which shows that the MU-HMIMOS channel exhibits spatial correlation. In addition, the smaller spacing among patch antennas, the more uneven the coupling coefficients and the steeper the eigenvalues decay, which implies stronger correlation. Specifically, the curve with

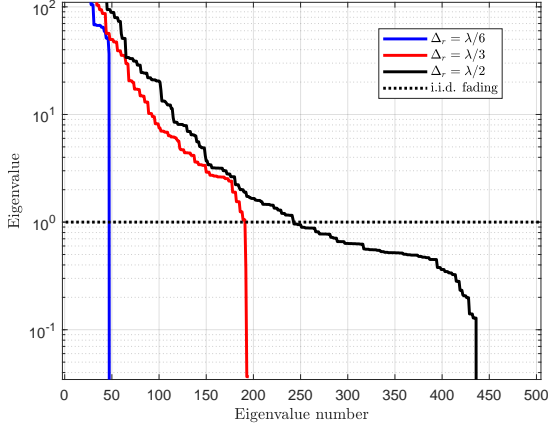


Figure 4: The eigenvalues of \mathbf{R} in decreasing order for MU-HMIMOS communication system with $N_s = 900$, $N_r = 576$, $\Delta_s = \lambda/3$ and $\Delta_r \in \{\lambda/6, \lambda/3, \lambda/2\}$.

$\Delta_r = \lambda/2$ decays much slower than that with $\Delta_r = \lambda/6$. The i.i.d. Rayleigh is also showed in black dot curve as reference. We can see from the figure that none of the curves resembles the reference case, even the curve $\Delta_r = \lambda/2$ that is the closest one still has a major difference. These observations all prove that an EM channel in MU-HMIMOS systems should not adopt i.i.d. Rayleigh fading modeling.

Fig. 5 shows the SE of ZF precoding and theoretical ZF precoding schemes with $N_r = 144$, $\Delta_s = \Delta = \lambda/3$ for different number of transmit patch antennas, and MMSE precoding scheme is set as benchmark curve. As shown in figure, there is very small gap between the ZF precoding and theoretical ZF schemes. Specifically, at lower SNR, the theoretical ZF perfectly predict the ZF precoding scheme. Thus, the effectiveness of the presented theoretical capacity is proved. Naturally, the more transmit patch antennas bring more benefits in SE. This can be accounted for that transmit surface is larger with the increase of patch antennas given the fixed spacing. What's more, the gap between ZF precoding and benchmark MMSE precoding is narrower with the increase of transmit patch antennas in high SNR region. This is mainly because the noise has little impact on ZF precoding when SNR goes high.

The SE of MRT precoding and theoretical MRT precoding schemes with $N_r = 144$, $\Delta_s = \Delta = \lambda/3$ for different number of transmit patch antennas are given in Fig. 6. The similar conclusion drawn from Fig. 5 can also be obtained in Fig. 6, i.e., the theoretical MRT can predict MRT precoding scheme in all SNR regions. Shown in the figure, the curves for $N_s = 144$ reach plateau at SNR=10 dB, this is because MRT shows advantages when the noise is dominant. With the increase of transmit patch antennas, not only the SE increases, the point to reach plateau also moves further. Thus, the increase of patch antennas generates larger transmit surface, and the MRT precoding has a better SE, thus it also reaches plateau at higher SNR region.

The impact of received patch antennas on the SE of MRT, ZF and MMSE precoding schemes for $N_s = 900$, $\Delta_s = \Delta = \lambda/6$ is given in Fig. 7. As shown in figure, the MRT precoding

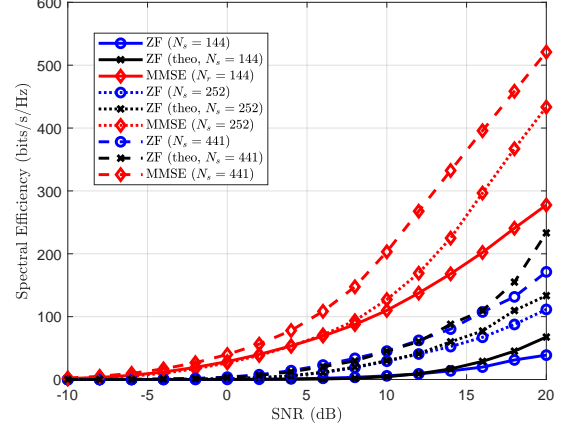


Figure 5: SE of ZF precoding, theoretical ZF precoding and MMSE precoding schemes for different transmit patch antennas with $N_r = 144$, $\Delta_s = \Delta_r = \lambda/3$.

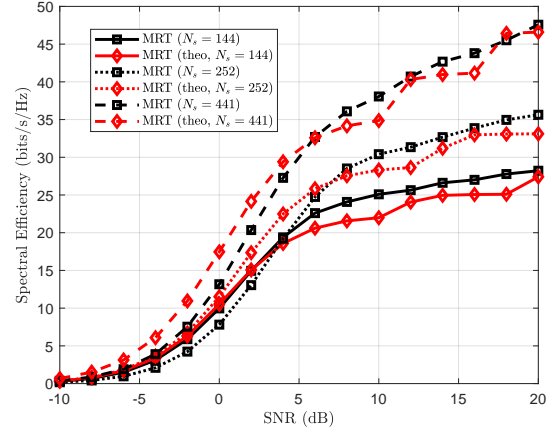


Figure 6: SE of MRT precoding scheme for different transmit patch antennas with $N_r = 144$, $\Delta_s = \Delta_r = \lambda/3$.

is better than ZF precoding in the low SNR region, which is contrary to the case in the high SNR region. This is mainly due to the noise, i.e., the noise is dominant in low SNR region, thus, MRT is better, while the noise impact is finite in the high SNR region, thus, ZF is better. As a benchmark, MMSE performs the best in the whole SNR region, and the gap between ZF and MMSE gradually decreases with the increase of SNR. In addition, the more received patch antennas bring benefits in SE. As observed from figure, the case $N_r = 288$ achieves the best performance compared with $N_r = 72$ and $N_r = 144$. This can be accounted for the larger received surface area enlarged by more received patch antennas under the fixed spacing.

The impact of transmit spacing on SE for MMSE, ZF, theoretical ZF, MRT and theoretical MRT precoding schemes are given in Fig. 8 and Fig. 9, respectively, under the settings of $N_s = 3600$, $N_r = 144$, $\Delta_r = \lambda/3$. From the Fig. 8, smaller spacing with giving number of patch antennas has less surface area and induces more correlation among patch antennas, thus, the SE is worse. Specifically, the ZF precoding scheme with $\Delta = \lambda/15$ has worse performance than $\Delta = \lambda/6$. In other words, there is a large reduction in correlated channel with larger spacing. Normally, the spacing $\Delta_s = \Delta_r = \lambda/2$

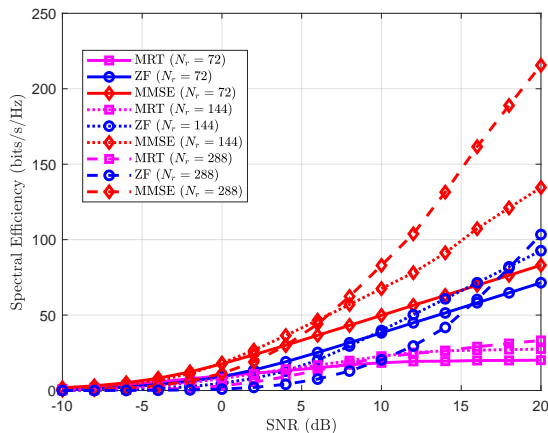


Figure 7: SE of MRT, ZF and MMSE precoding schemes for different received patch antennas with $N_s = 900$, $\Delta_s = \Delta_r = \lambda/6$.

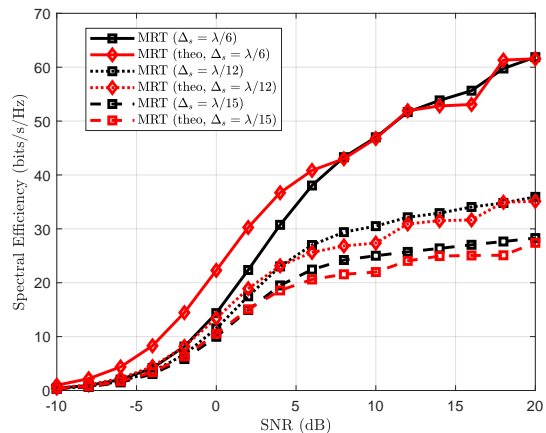


Figure 9: SE of MRT precoding schemes for different spacing with $N_s = 3600$, $N_r = 144$, $\Delta_r = \lambda/3$.

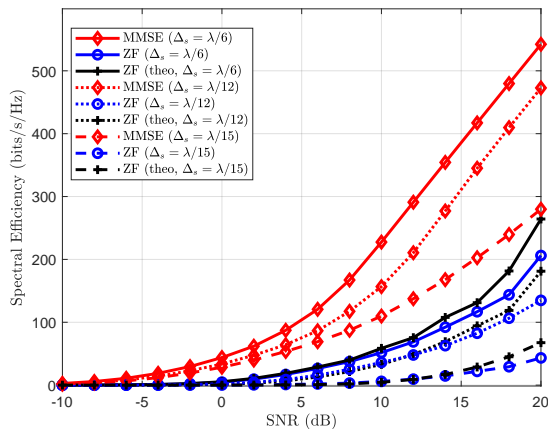


Figure 8: SE of ZF and MMSE precoding schemes for different spacing with $N_s = 3600$, $N_r = 144$, $\Delta_r = \lambda/3$.

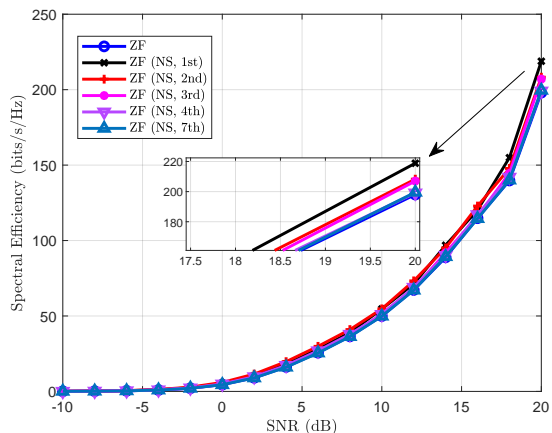


Figure 10: Comparison of ZF precoding scheme and NS based ZF precoding for different iterations with $N_s = 729$, $N_r = 144$, $\Delta_s = \Delta_r = \lambda/3$.

is adopted in the uncorrelated channel assumption for SE analysis [12]. In addition, the theoretical ZF with closer spacing predicts the ZF precoding well, thus, the presented theoretical ZF could perform well in highly correlated cases. The similar observation is also obtained in Fig. 9. Specifically, the theoretical MRT with $\Delta_s = \lambda/15$ predicts that the performance of MRT is better than the case $\Delta_s = \lambda/6$ in the whole SNR region. Both figures show that less spacing has a lower SE and the proposed theoretical analyses perform well in highly correlated cases.

Fig. 10 shows the impact of iteration on the SE for NS based ZF precoding scheme with $N_s = 729$, $N_r = 144$ and $\Delta_s = \Delta_r = \lambda/3$. As mentioned before, the NS scheme avoids the computationally expensive matrix inversion operation using iterative methods. Shown in the figure, the ZF precoding employing NS with more iterations is closer to the ZF precoding scheme. Specifically, the case with 4-th iteration almost coincides that with 7-th iteration, and there is also just a narrow gap between 4-th iteration and 3-rd iteration. Thus, we normally adopt 4 iterations in practical simulations for achieving a balance between the computational cost and performance.

V. CONCLUSION

In this paper, we presented the channel modeling in MU-HMIMOS communication systems. Specifically, the constructed EM channel is mainly composed of the wavenumber domain channel that is dependent on the amount and spacing of patch antennas. We also analytically investigated the MRT and ZF precoding schemes, and the corresponding theoretical SE were derived. Furthermore, a low complexity NS method for ZF precoding scheme was proposed to replace the involved matrix inversion that is impractical in MU-HMIMOS systems due to the extremely large number of patch antennas. Our simulation results verified that the more patch antennas in both transmitter and receiver with the fixed spacing generate a better SE for a larger surface area, but the closer spacing induces the stronger correlation in system, which can impair the performance of SE for different precoding schemes. Finally, it can be seen that the proposed NS based ZF precoding can achieve a similar performance with ZF precoding scheme with more iterations without matrix inversion.

APPENDIX

Here we compute the variance of the received response assuming the isotropic environment, where $A = \frac{2\pi}{\sqrt{k}}$ and

$k = \frac{2\pi}{\lambda}$, $\ell_x = -L_{x,y}/\lambda, \dots, L_{r,x}/\lambda - 1$ and $\ell_y = -L_{r,y}/\lambda, \dots, L_{r,y}/\lambda - 1$.

1) *The first orthant* $\phi_r \in [0, \pi/2)$: In the first orthant, we have $\phi_{r,1} = \arctan \frac{c}{b}$, $\phi_{r,2} = \min(\arctan \frac{c}{a}, \arctan \frac{d}{b})$, $\phi_{r,3} = \max(\arctan \frac{d}{b}, \arctan \frac{c}{a})$, $\phi_{r,4} = \arctan \frac{d}{a}$. The three subregions parameterized by θ_r are given by:

$\Omega_{r,1} : \theta_{r,\min}(\phi_r) = \arcsin(\min(1, \frac{c}{\sin \phi_r}))$, $\theta_{r,\max}(\phi_r) = \arcsin(\min(1, \frac{b}{\cos \phi_r}))$;

$\Omega_{r,2}(\ell_x > \ell_y) : \theta_{r,\min}(\phi_r) = \arcsin(\min(1, \frac{a}{\cos \phi_r}))$, $\theta_{r,\max}(\phi_r) = \arcsin(\min(1, \frac{b}{\cos \phi_r}))$;

$\Omega_{r,2}(\ell_x \leq \ell_y) : \theta_{r,\min}(\phi_r) = \arcsin(\min(1, \frac{c}{\sin \phi_r}))$, $\theta_{r,\max}(\phi_r) = \arcsin(\min(1, \frac{d}{\sin \phi_r}))$;

$\Omega_{r,3} : \theta_{r,\min}(\phi_r) = \arcsin(\min(1, \frac{a}{\cos \phi_r}))$, $\theta_{r,\max}(\phi_r) = \arcsin(\min(1, \frac{d}{\sin \phi_r}))$.

$\ell_x > \ell_y, \phi_r \in [0, \pi/2) :$

$$\begin{aligned}
\sigma_r^2(\ell_x, \ell_y) &= \iint_{\Omega_r(\ell_x, \ell_y)} A^2(\theta_r, \phi_r) dk_r d\phi_r \\
&= \frac{1}{4\pi} \sum_{i=1}^3 \iint_{\Omega_{r,i}(\ell_x, \ell_y)} \frac{k_r}{\sqrt{1-k_r^2}} dk_r d\phi_r \\
&= \int_{\phi_{r,1}}^{\phi_{r,2}} \int_{\min(1, \frac{c}{\sin \phi_r})}^{\min(1, \frac{b}{\cos \phi_r})} \frac{k_r}{\sqrt{1-k_r^2}} dk_r d\phi_r \\
&\quad + \int_{\phi_{r,2}}^{\phi_{r,3}} \int_{\min(1, \frac{a}{\cos \phi_r})}^{\min(1, \frac{b}{\cos \phi_r})} \frac{k_r}{\sqrt{1-k_r^2}} dk_r d\phi_r \\
&\quad + \int_{\phi_{r,3}}^{\phi_{r,4}} \int_{\min(1, \frac{a}{\cos \phi_r})}^{\min(1, \frac{d}{\sin \phi_r})} \frac{k_r}{\sqrt{1-k_r^2}} dk_r d\phi_r \\
&= \int_{\phi_{r,1}}^{\phi_{r,2}} \sqrt{1 - \min(1, \frac{c^2}{\sin^2 \phi_r})} d\phi_r \\
&\quad - \int_{\phi_{r,1}}^{\phi_{r,2}} \sqrt{1 - \min(1, \frac{b^2}{\cos^2 \phi_r})} d\phi_r \\
&\quad + \int_{\phi_{r,2}}^{\phi_{r,3}} \sqrt{1 - \min(1, \frac{a^2}{\cos^2 \phi_r})} d\phi_r \\
&\quad - \int_{\phi_{r,2}}^{\phi_{r,3}} \sqrt{1 - \min(1, \frac{b^2}{\cos^2 \phi_r})} dk_r d\phi_r \\
&\quad + \int_{\phi_{r,3}}^{\phi_{r,4}} \sqrt{1 - \min(1, \frac{a^2}{\cos^2 \phi_r})} d\phi_r \\
&\quad - \int_{\phi_{r,3}}^{\phi_{r,4}} \sqrt{1 - \min(1, \frac{d^2}{\sin^2 \phi_r})} dk_r d\phi_r \\
&= \int_{\max(\phi_{r,1}, \arcsin c)}^{\max(\phi_{r,2}, \arcsin c)} \sqrt{1 - \frac{c^2}{\sin^2 \phi_r}} d\phi_r \\
&\quad - \int_{\min(\phi_{r,1}, \arccos b)}^{\min(\phi_{r,2}, \arccos b)} \sqrt{1 - \frac{b^2}{\cos^2 \phi_r}} d\phi_r \\
&\quad + \int_{\min(\phi_{r,2}, \arccos a)}^{\min(\phi_{r,3}, \arccos a)} \sqrt{1 - \frac{a^2}{\cos^2 \phi_r}} d\phi_r \\
&\quad - \int_{\min(\phi_{r,2}, \arccos b)}^{\min(\phi_{r,3}, \arccos b)} \sqrt{1 - \frac{b^2}{\cos^2 \phi_r}} dk_r d\phi_r
\end{aligned} \tag{49}$$

$$\begin{aligned}
&+ \int_{\min(\phi_{r,3}, \arccos a)}^{\min(\phi_{r,4}, \arccos a)} \sqrt{1 - \frac{a^2}{\cos^2 \phi_r}} d\phi_r \\
&- \int_{\max(\phi_{r,3}, \arcsin d)}^{\max(\phi_{r,4}, \arcsin d)} \sqrt{1 - \frac{d^2}{\sin^2 \phi_r}} dk_r d\phi_r,
\end{aligned}$$

where $a = \frac{\lambda \ell_x}{L_{r,x}}$, $b = \frac{\lambda(\ell_x+1)}{L_{r,x}}$, $c = \frac{\lambda \ell_y}{L_{r,y}}$, $d = \frac{\lambda(\ell_y+1)}{L_{r,y}}$, and

$$\begin{aligned}
\mathcal{E}_r &= \left\{ (\ell_x, \ell_y) \in \mathbb{Z}^2 : (\ell_x \lambda / L_{r,x})^2 + (\ell_y \lambda / L_{r,y})^2 \leq 1 \right\}. \\
|\mathcal{E}_r| &= n_r, \quad n_r = \left\lfloor \frac{\pi}{\lambda^2} L_{r,x} L_{r,y} \right\rfloor. \\
\ell_x &= -\frac{L_{r,x}/\lambda-1}{2}, \dots, \frac{L_{r,x}/\lambda-1}{2} - 1, \quad \ell_y = \\
&-\frac{L_{r,y}/\lambda-1}{2}, \dots, \frac{L_{r,y}/\lambda-1}{2} - 1.
\end{aligned}$$

We have [44]

$$\begin{aligned}
&\int_{\max(\phi_{r,1}, \arcsin c)}^{\max(\phi_{r,2}, \arcsin c)} \sqrt{1 - \frac{c^2}{\sin^2 \phi_r}} d\phi_r = c \arctan \left(\frac{\cos \phi_r}{\sqrt{\frac{\sin^2 \phi_r}{c^2} - 1}} \right) \\
&\quad - \frac{1}{c} \arcsin \left(\frac{\cos \phi_r}{\sqrt{1 - c^2}} \right) \Big|_{\max(\phi_{r,1}, \arcsin c)}^{\max(\phi_{r,2}, \arcsin c)}, \\
&\int_{\min(\phi_{r,1}, \arccos b)}^{\min(\phi_{r,2}, \arccos b)} \sqrt{1 - \frac{b^2}{\cos^2 \phi_r}} d\phi_r = -b \arctan \left(\frac{\sin \phi_r}{\sqrt{\frac{\cos^2 \phi_r}{b^2} - 1}} \right) \\
&\quad + \arcsin \left(\frac{\sin \phi_r}{\sqrt{1 - b^2}} \right) \Big|_{\min(\phi_{r,1}, \arccos b)}^{\min(\phi_{r,2}, \arccos b)}.
\end{aligned} \tag{50}$$

Similarly, for $\ell_x \leq \ell_y, \phi_r \in [0, \pi/2) :$

$$\begin{aligned}
\sigma_r^2(\ell_x, \ell_y) &= \int_{\phi_{r,1}}^{\phi_{r,2}} \int_{\min(1, \frac{c}{\sin \phi_r})}^{\min(1, \frac{b}{\cos \phi_r})} \frac{k_r}{\sqrt{1-k_r^2}} dk_r d\phi_r \\
&\quad + \int_{\phi_{r,2}}^{\phi_{r,3}} \int_{\min(1, \frac{c}{\sin \phi_r})}^{\min(1, \frac{d}{\sin \phi_r})} \frac{k_r}{\sqrt{1-k_r^2}} dk_r d\phi_r \\
&\quad + \int_{\phi_{r,3}}^{\phi_{r,4}} \int_{\min(1, \frac{a}{\cos \phi_r})}^{\min(1, \frac{d}{\sin \phi_r})} \frac{k_r}{\sqrt{1-k_r^2}} dk_r d\phi_r.
\end{aligned} \tag{51}$$

2) *Second orthant* $\phi_r \in [\pi/2, \pi)$: In the second orthant, we have $\phi_{r,1} = \pi - \arctan \frac{d}{|b|}$, $\phi_{r,2} = \pi - \max(\arctan \frac{c}{|b|}, \arctan \frac{d}{|a|})$, $\phi_{r,3} = \pi - \min(\arctan \frac{c}{|b|}, \arctan \frac{d}{|a|})$, $\phi_{r,4} = \pi - \arctan \frac{c}{|a|}$. The three subregions parameterized by θ_r are given by:

$\Omega_{r,1} : \theta_{r,\min}(\phi_r) = \arcsin(\min(1, \frac{|b|}{\cos(\pi-\phi_r)}))$, $\theta_{r,\max}(\phi_r) = \arcsin(\min(1, \frac{d}{\sin(\pi-\phi_r)}))$;

$\Omega_{r,2}(|\ell_x| > \ell_y) : \theta_{r,\min}(\phi_r) = \arcsin(\min(1, \frac{|b|}{\cos(\pi-\phi_r)}))$, $\theta_{r,\max}(\phi_r) = \arcsin(\min(1, \frac{|a|}{\cos(\pi-\phi_r)}))$;

$\Omega_{r,2}(|\ell_x| \leq \ell_y) : \theta_{r,\min}(\phi_r) = \arcsin(\min(1, \frac{c}{\sin(\pi-\phi_r)}))$, $\theta_{r,\max}(\phi_r) = \arcsin(\min(1, \frac{d}{\sin(\pi-\phi_r)}))$;

$\Omega_{r,3} : \theta_{r,\min}(\phi_r) = \arcsin(\min(1, \frac{c}{\sin(\pi-\phi_r)}))$, $\theta_{r,\max}(\phi_r) = \arcsin(\min(1, \frac{|a|}{\cos(\pi-\phi_r)}))$.

$|\ell_x| > \ell_y, \phi_r \in [\pi/2, \pi) :$

$$\begin{aligned}
\sigma_r^2(\ell_x, \ell_y) &= \int_{\phi_{r,1}}^{\phi_{r,2}} \int_{\min(1, \frac{|b|}{\cos \phi_r})}^{\min(1, \frac{d}{\sin \phi_r})} \frac{k_r}{\sqrt{1-k_r^2}} dk_r d\phi_r \\
&\quad + \int_{\phi_{r,2}}^{\phi_{r,3}} \int_{\min(1, \frac{|a|}{\cos \phi_r})}^{\min(1, \frac{d}{\sin \phi_r})} \frac{k_r}{\sqrt{1-k_r^2}} dk_r d\phi_r
\end{aligned} \tag{52}$$

$$+ \int_{\phi_{r,3}}^{\phi_{r,4}} \int_{\min(1, \frac{|a|}{\cos \phi_r})}^{\min(1, \frac{|a|}{\sin \phi_r})} \frac{k_r}{\sqrt{1-k_r^2}} dk_r d\phi_r.$$

$|\ell_x| \leq |\ell_y|, \phi_r \in [\pi/2, \pi) :$

$$\begin{aligned} \sigma_r^2(\ell_x, \ell_y) &= \int_{\phi_{r,1}}^{\phi_{r,2}} \int_{\min(1, \frac{|d|}{\sin \phi_r})}^{\min(1, \frac{d}{\sin \phi_r})} \frac{k_r}{\sqrt{1-k_r^2}} dk_r d\phi_r \\ &+ \int_{\phi_{r,2}}^{\phi_{r,3}} \int_{\min(1, \frac{c}{\sin \phi_r})}^{\min(1, \frac{d}{\sin \phi_r})} \frac{k_r}{\sqrt{1-k_r^2}} dk_r d\phi_r \\ &+ \int_{\phi_{r,3}}^{\phi_{r,4}} \int_{\min(1, \frac{c}{\sin \phi_r})}^{\min(1, \frac{|a|}{\cos \phi_r})} \frac{k_r}{\sqrt{1-k_r^2}} dk_r d\phi_r. \end{aligned} \quad (53)$$

3) *Third orthant* $\phi_r \in [\pi, 3\pi/2)$: In the third orthant, we have $\phi_{r,1} = \pi + \arctan \frac{|d|}{|a|}$, $\phi_{r,2} = \pi + \min(\arctan \frac{|d|}{|b|}, \arctan \frac{|c|}{|a|})$, $\phi_{r,3} = \pi + \max(\arctan \frac{|d|}{|b|}, \arctan \frac{|c|}{|a|})$, $\phi_{r,4} = \pi + \arctan \frac{|c|}{|b|}$. The three subregions parameterized by θ_r are given by:

$\Omega_{r,1} : \theta_{r,\min}(\phi_r) = \arcsin(\min(1, \frac{|d|}{\sin(\phi_r-\pi)}))$, $\theta_{r,\max}(\phi_r) = \arcsin(\min(1, \frac{|a|}{\cos(\phi_r-\pi)}))$;

$\Omega_{r,2}(|\ell_x| > |\ell_y|) : \theta_{r,\min}(\phi_r) = \arcsin(\min(1, \frac{|b|}{\cos(\phi_r-\pi)}))$, $\theta_{r,\max}(\phi_r) = \arcsin(\min(1, \frac{|a|}{\cos(\phi_r-\pi)}))$;

$\Omega_{r,2}(|\ell_x| \leq |\ell_y|) : \theta_{r,\min}(\phi_r) = \arcsin(\min(1, \frac{|d|}{\sin(\phi_r-\pi)}))$, $\theta_{r,\max}(\phi_r) = \arcsin(\min(1, \frac{|c|}{\sin(\phi_r-\pi)}))$;

$\Omega_{r,3} : \theta_{r,\min}(\phi_r) = \arcsin(\min(1, \frac{|b|}{\cos(\phi_r-\pi)}))$, $\theta_{r,\max}(\phi_r) = \arcsin(\min(1, \frac{|c|}{\sin(\phi_r-\pi)}))$.

$|\ell_x| > |\ell_y|, \phi_r \in [\pi, 3\pi/2) :$

$$\begin{aligned} \sigma_r^2(\ell_x, \ell_y) &= \int_{\phi_{r,1}}^{\phi_{r,2}} \int_{\min(1, \frac{|a|}{\cos \phi_r})}^{\min(1, \frac{|a|}{\sin \phi_r})} \frac{k_r}{\sqrt{1-k_r^2}} dk_r d\phi_r \\ &+ \int_{\phi_{r,2}}^{\phi_{r,3}} \int_{\min(1, \frac{|b|}{\cos \phi_r})}^{\min(1, \frac{|a|}{\cos \phi_r})} \frac{k_r}{\sqrt{1-k_r^2}} dk_r d\phi_r \\ &+ \int_{\phi_{r,3}}^{\phi_{r,4}} \int_{\min(1, \frac{|b|}{\cos \phi_r})}^{\min(1, \frac{|c|}{\sin \phi_r})} \frac{k_r}{\sqrt{1-k_r^2}} dk_r d\phi_r. \end{aligned} \quad (54)$$

$|\ell_x| \leq |\ell_y|, \phi_r \in [\pi, 3\pi/2) :$

$$\begin{aligned} \sigma_r^2(\ell_x, \ell_y) &= \int_{\phi_{r,1}}^{\phi_{r,2}} \int_{\min(1, \frac{|a|}{\cos \phi_r})}^{\min(1, \frac{|a|}{\sin \phi_r})} \frac{k_r}{\sqrt{1-k_r^2}} dk_r d\phi_r \\ &+ \int_{\phi_{r,2}}^{\phi_{r,3}} \int_{\min(1, \frac{|d|}{\sin \phi_r})}^{\min(1, \frac{|c|}{\sin \phi_r})} \frac{k_r}{\sqrt{1-k_r^2}} dk_r d\phi_r \\ &+ \int_{\phi_{r,3}}^{\phi_{r,4}} \int_{\min(1, \frac{|b|}{\cos \phi_r})}^{\min(1, \frac{|c|}{\sin \phi_r})} \frac{k_r}{\sqrt{1-k_r^2}} dk_r d\phi_r. \end{aligned} \quad (55)$$

4) *Fourth orthant* $\phi_r \in [3\pi/2, 2\pi)$: In the fourth orthant, we have $\phi_{r,1} = 2\pi - \arctan \frac{|c|}{|a|}$, $\phi_{r,2} = 2\pi - \max(\arctan \frac{|d|}{|a|}, \arctan \frac{|c|}{|b|})$, $\phi_{r,3} = 2\pi - \min(\arctan \frac{|d|}{|a|}, \arctan \frac{|c|}{|b|})$, $\phi_{r,4} = 2\pi - \arctan \frac{|d|}{|b|}$. The three subregions parameterized by θ_r are given by:

$\Omega_{r,1} : \theta_{r,\min}(\phi_r) = \arcsin(\min(1, \frac{a}{\cos(2\pi-\phi_r)}))$, $\theta_{r,\max}(\phi_r) = \arcsin(\min(1, \frac{|c|}{\sin(2\pi-\phi_r)}))$;

$\Omega_{r,2}(|\ell_x| > |\ell_y|) : \theta_{r,\min}(\phi_r) = \arcsin(\min(1, \frac{a}{\cos(2\pi-\phi_r)}))$,

$\theta_{r,\max}(\phi_r) = \arcsin(\min(1, \frac{b}{\cos(2\pi-\phi_r)}))$;

$\Omega_{r,2}(|\ell_x| \leq |\ell_y|) : \theta_{r,\min}(\phi_r) = \arcsin(\min(1, \frac{|d|}{\sin(2\pi-\phi_r)}))$,

$\theta_{r,\max}(\phi_r) = \arcsin(\min(1, \frac{|c|}{\sin(2\pi-\phi_r)}))$;

$\Omega_{r,3} : \theta_{r,\min}(\phi_r) = \arcsin(\min(1, \frac{|d|}{\sin(2\pi-\phi_r)}))$, $\theta_{r,\max}(\phi_r) = \arcsin(\min(1, \frac{b}{\cos(2\pi-\phi_r)}))$.

$|\ell_x| > |\ell_y|, \phi_r \in [3\pi/2, 2\pi) :$

$$\begin{aligned} \sigma_r^2(\ell_x, \ell_y) &= \int_{\phi_{r,1}}^{\phi_{r,2}} \int_{\min(1, \frac{|c|}{\sin \phi_r})}^{\min(1, \frac{|c|}{\sin \phi_r})} \frac{k_r}{\sqrt{1-k_r^2}} dk_r d\phi_r \\ &+ \int_{\phi_{r,2}}^{\phi_{r,3}} \int_{\min(1, \frac{a}{\cos \phi_r})}^{\min(1, \frac{b}{\cos \phi_r})} \frac{k_r}{\sqrt{1-k_r^2}} dk_r d\phi_r \\ &+ \int_{\phi_{r,3}}^{\phi_{r,4}} \int_{\min(1, \frac{|d|}{\sin \phi_r})}^{\min(1, \frac{b}{\cos \phi_r})} \frac{k_r}{\sqrt{1-k_r^2}} dk_r d\phi_r. \end{aligned} \quad (56)$$

$|\ell_x| \leq |\ell_y|, \phi_r \in [3\pi/2, 2\pi) :$

$$\begin{aligned} \sigma_r^2(\ell_x, \ell_y) &= \int_{\phi_{r,1}}^{\phi_{r,2}} \int_{\min(1, \frac{|c|}{\sin \phi_r})}^{\min(1, \frac{|c|}{\sin \phi_r})} \frac{k_r}{\sqrt{1-k_r^2}} dk_r d\phi_r \\ &+ \int_{\phi_{r,2}}^{\phi_{r,3}} \int_{\min(1, \frac{|d|}{\sin \phi_r})}^{\min(1, \frac{|c|}{\sin \phi_r})} \frac{k_r}{\sqrt{1-k_r^2}} dk_r d\phi_r \\ &+ \int_{\phi_{r,3}}^{\phi_{r,4}} \int_{\min(1, \frac{|d|}{\sin \phi_r})}^{\min(1, \frac{b}{\cos \phi_r})} \frac{k_r}{\sqrt{1-k_r^2}} dk_r d\phi_r. \end{aligned} \quad (57)$$

REFERENCES

- [1] Z. Wan, Z. Gao, F. Gao, M. Di Renzo, and M. Alouini, "Terahertz massive MIMO with holographic reconfigurable intelligent surfaces," *IEEE Trans. Commun.*, vol. 69, no. 7, pp. 4732–4750, Jul. 2021.
- [2] B. Ning, Z. Chen, W. Chen, Y. Du, and J. Fang, "Terahertz multi-user massive MIMO with intelligent reflecting surface: Beam training and hybrid beamforming," *IEEE Trans. Veh. Tech.*, vol. 70, no. 2, pp. 1376–1393, Feb. 2021.
- [3] I. F. Akyildiz, C. Han, and S. Nie, "Combating the distance problem in the millimeter wave and terahertz frequency bands," *IEEE Commun. Mag.*, vol. 56, no. 6, pp. 102–108, Jun. 2018.
- [4] N. Shlezinger, G. C. Alexandropoulos, M. F. Imani, Y. C. Eldar, and D. R. Smith, "Dynamic metasurface antennas for 6G extreme massive MIMO communications," *IEEE Wireless Commun.*, vol. 28, no. 2, pp. 106–113, Jan. 2021.
- [5] D. Dardari and N. Decarli, "Holographic communication using intelligent surfaces," *IEEE Commun. Mag.*, vol. 59, no. 6, pp. 35–41, Jun. 2021.
- [6] T. H. Nguyen, T. V. Chien, H. Q. Ngo, X. N. Tran, and E. Björnson, "Pilot assignment for joint uplink-downlink spectral efficiency enhancement in massive MIMO systems with spatial correlation," *IEEE Trans. Veh. Tech.*, vol. 70, no. 8, pp. 8292–8297, 2021.
- [7] T. J. Willink, "Efficient adaptive SVD algorithm for MIMO applications," *IEEE Trans. Signal Processing*, vol. 56, no. 2, pp. 615–622, Feb. 2008.
- [8] M. Di Renzo, H. Haas, A. Ghayeb, S. Sugiura, and L. Hanzo, "Spatial modulation for generalized MIMO: Challenges, opportunities, and implementation," *Proc. IEEE*, vol. 102, no. 1, pp. 56–103, Jan. 2014.
- [9] R. Zhang and C. K. Ho, "MIMO broadcasting for simultaneous wireless information and power transfer," *IEEE Trans. Wirel. Commun.*, vol. 12, no. 5, pp. 1989–2001, May 2013.
- [10] X. Liu, T. Huang, N. Shlezinger, Y. Liu, J. Zhou, and Y. C. Eldar, "Joint transmit beamforming for multiuser MIMO communications and MIMO radar," *IEEE Trans. Signal Processing*, vol. 68, pp. 3929–3944, Feb. 2020.
- [11] H. Huh, G. Caire, H. C. Papadopoulos, and S. A. Ramprasad, "Achieving "Massive MIMO" spectral efficiency with a not-so-large number of antennas," *IEEE Trans. Wirel. Commun.*, vol. 11, no. 9, pp. 3226–3239, Sept. 2012.

- [12] H. Q. Ngo, E. G. Larsson, and T. L. Marzetta, "Energy and spectral efficiency of very large multiuser MIMO systems," *IEEE Trans. Commun.*, vol. 61, no. 4, pp. 1436–1449, Apr. 2013.
- [13] E. Björnson, L. Sanguinetti, and J. Hoydis, "Hardware distortion correlation has negligible impact on UL massive MIMO spectral efficiency," *IEEE Trans. Commun.*, vol. 67, no. 2, pp. 1085–1098, Feb. 2019.
- [14] A. A. Amin and S. Y. Shin, "Capacity analysis of cooperative NOMA-OAM-MIMO based full-duplex relaying for 6G," *IEEE Wirel. Commun. Lett.*, vol. 10, no. 7, pp. 1395–1399, Jul. 2021.
- [15] H. Fu, S. Roy, and L. Peng, "Asymptotic performance analysis of MMSE receivers in multicell MU-MIMO systems," *IEEE Trans. Veh. Tech.*, vol. 70, no. 9, pp. 9174–9189, Sept. 2021.
- [16] L. Yang, Y. Jinxia, W. Xie, M. Hasna, T. Tsiftsis, and M. Di Renzo, "Secrecy performance analysis of RIS-aided wireless communication systems," *IEEE Trans. Veh. Tech.*, early access, 2020.
- [17] G. C. Alexandropoulos, K. Katsanos, M. Wen, and D. B. da Costa, "Safeguarding MIMO communications with reconfigurable metasurfaces and artificial noise," in *in Proc. IEEE ICC*, 2021, pp. 1–6.
- [18] H. Wang, J. Bai, and L. Dong, "Intelligent reflecting surfaces assisted secure transmission without eavesdropper's CSI," *IEEE Signal Process. Letters*, early access, 2020.
- [19] X. Guan, Q. Wu, and R. Zhang, "Intelligent reflecting surface assisted secrecy communication: Is artificial noise helpful or not?," *IEEE Wireless Commun. Lett.*, vol. 9, no. 6, pp. 778–782, Jun. 2020.
- [20] C. Pan, H. Ren, K. Wang, J. Kolb, M. ElKashlan, M. Chen, M. Di Renzo, Y. Hao, J. Wang, A. L. Swindlehurst, X. You, and L. Hanzo, "Reconfigurable intelligent surfaces for 6G systems: Principles, applications, and research directions," *IEEE Commun. Mag.*, vol. 59, no. 6, pp. 14–20, Jun. 2021.
- [21] O. Yurduseven, D. L. Marks, T. Fromenteze, and D. R. Smith, "Dynamically reconfigurable holographic metasurface aperture for a Mills-Cross monochromatic microwave camera," *Opt. Express*, vol. 26, no. 5, pp. 5281–5291, 2018.
- [22] C. Huang, A. Zappone, G. C. Alexandropoulos, M. Debbah, and C. Yuen, "Reconfigurable intelligent surfaces for energy efficiency in wireless communication," *IEEE Trans. Wireless Commun.*, vol. 18, no. 8, pp. 4157–4170, Aug. 2019.
- [23] M. Di Renzo, K. Ntontin, J. Song, F. H. Danufane, X. Qian, F. Lazarakis, J. De Rosny, D. Phan-Huy, O. Simeone, R. Zhang, M. Debbah, G. Lerosey, M. Fink, S. Tretjakov, and S. Shamai, "Reconfigurable intelligent surfaces vs. relaying: Differences, similarities, and performance comparison," *IEEE OJ-COMS*, vol. 1, pp. 798–807, Jun. 2020.
- [24] S. Hu, F. Rusek, and O. Edfors, "Beyond massive MIMO: The potential of data-transmission with large intelligent surfaces," *IEEE Trans. Signal Process.*, vol. 66, no. 10, pp. 2746–2758, May 2018.
- [25] C. Liaskos, S. Nie, A. Tsioliaridou, A. Pitsillides, S. Ioannidis, and I. F. Akyildiz, "A new wireless communication paradigm through software-controlled metasurfaces," *IEEE Commun. Mag.*, vol. 56, no. 9, pp. 162–169, Sep. 2018.
- [26] Q. Wu and R. Zhang, "Towards smart and reconfigurable environment: Intelligent reflecting surface aided wireless network," *IEEE Commun. Mag.*, vol. 58, no. 1, Jan. 2020.
- [27] G. C. Alexandropoulos, G. Lerosey, M. Debbah, and M. Fink, "Reconfigurable intelligent surfaces and metamaterials: The potential of wave propagation control for 6G wireless communications," *IEEE ComSoc TCCN Newsl.*, vol. 6, no. 1, pp. 25–37, Jun. 2020, [Online] <https://arxiv.org/pdf/2006.11136>.
- [28] W. Tang, M. Chen, X. Chen, J. Dai, Y. Han, M. D. Renzo, Y. Zeng, S. Jin, Q. Cheng, and T. Cui, "Wireless communications with reconfigurable intelligent surface: Path loss modeling and experimental measurement," *IEEE Trans. Wirel. Commun.*, vol. 20, no. 1, pp. 421–439, Jan. 2021.
- [29] C. Pan, H. Ren, K. Wang, M. ElKashlan, A. Nallanathan, J. Wang, and L. Hanzo, "Intelligent reflecting surface aided MIMO broadcasting for simultaneous wireless information and power transfer," *IEEE J. Sel. Areas Commun.*, vol. 38, no. 8, pp. 1719–1734, Aug. 2020.
- [30] T. Bai, C. Pan, H. Ren, Y. Deng, M. ElKashlan, and A. Nallanathan, "Resource allocation for intelligent reflecting surface aided wireless powered mobile edge computing in OFDM systems," *IEEE Trans. Wirel. Commun.*, vol. 20, no. 8, pp. 5389–5407, Aug. 2021.
- [31] S. Hong, C. Pan, H. Ren, K. Wang, and A. Nallanathan, "Artificial-noise-aided secure MIMO wireless communications via intelligent reflecting surface," *IEEE Trans. Commun.*, vol. 68, no. 12, pp. 7851–7866, Dec. 2020.
- [32] M. Di Renzo, M. Debbah, D.-T. Phan-Huy, A. Zappone, M.-S. Alouini, C. Yuen, V. Sciancalepore, G. C. Alexandropoulos, J. Hoydis, H. Gacanin, J. de Rosny, A. Bounceur, G. Lerosey, and M. Fink, "Smart radio environments empowered by reconfigurable AI meta-surfaces: An idea whose time has come," *EURASIP J. Wireless Commun. Netw.*, vol. 2019, no. 1, pp. 1–20, May 2019.
- [33] G. Zhou, C. Pan, H. Ren, K. Wang, and A. Nallanathan, "A framework of robust transmission design for IRS-aided MISO communications with imperfect cascaded channels," *IEEE Trans. Signal Process.*, vol. 68, pp. 5092–5106, Aug. 2020.
- [34] C. Pan, H. Ren, K. Wang, W. Xu, M. ElKashlan, A. Nallanathan, and L. Hanzo, "Multicell MIMO communications relying on intelligent reflecting surfaces," *IEEE Trans. Wirel. Commun.*, vol. 19, no. 8, pp. 5218–5233, Aug. 2020.
- [35] W. Yan, X. Yuan, and X. Kuai, "Passive beamforming and information transfer via large intelligent surface," *IEEE Wirel. Commun. Lett.*, vol. 9, no. 4, pp. 533–537, Apr. 2020.
- [36] T. Hou, Y. Liu, Z. Song, X. Sun, Y. Chen, and L. Hanzo, "Reconfigurable intelligent surface aided NOMA networks," *IEEE J. Sel. Area. Comm.*, early access, 2020.
- [37] C. Huang, S. Hu, G. C. Alexandropoulos, A. Zappone, C. Yuen, R. Zhang, M. Di Renzo, and M. Debbah, "Holographic MIMO surfaces for 6G wireless networks: Opportunities, challenges, and trends," *IEEE Wirel. Commun.*, vol. 27, no. 5, pp. 118–125, Oct. 2020.
- [38] Ö. T. Demir, E. Björnson, and L. Sanguinetti, "Channel modeling and channel estimation for holographic massive MIMO with planar arrays," *arXiv preprint arXiv:2108.04633*, 2021.
- [39] E. Calvanese Strinati et al., "Reconfigurable, intelligent, and sustainable wireless environments for 6G smart connectivity," *IEEE Commun. Mag.*, to appear, 2021.
- [40] S. Basharat, S.A. Hassan, H. Pervaiz, A. Mahmood, Z. Ding, and M. Gidlund, "Reconfigurable intelligent surfaces: Potentials, applications, and challenges for 6G wireless networks," *IEEE Wirel. Commun.*, pp. 1–8, 2021.
- [41] R. J. Williams, E. de Carvalho, and T. L. Marzetta, "A communication model for large intelligent surfaces," in *2020 IEEE ICC Workshops*, 2020, pp. 1–6.
- [42] T. L. Marzetta, "Spatially-stationary propagating random field model for massive MIMO small-scale fading," in *2018 IEEE ISIT*, 2018, pp. 391–395.
- [43] L. Sanguinetti, A. A. D'Amico, and M. Debbah, "Wavenumber-division multiplexing in line-of-sight holographic MIMO communications," *arXiv preprint arXiv:2106.12531*, 2021.
- [44] A. Pizzo, T. L. Marzetta, and L. Sanguinetti, "Spatially-stationary model for holographic MIMO small-scale fading," *IEEE J. Sel. Areas Commun.*, vol. 38, no. 9, pp. 1964–1979, Sept. 2020.
- [45] A. Pizzo, T. L. Marzetta, and L. Sanguinetti, "Degrees of freedom of holographic MIMO channels," in *2020 IEEE 21st SPAWC*, 2020, pp. 1–5.
- [46] Q. Deng, X. Liang, X. Wang, M. Huang, C. Dong, and Y. Zhang, "Fast converging iterative precoding for massive MIMO systems: An accelerated weighted Neumann series-steepest descent approach," *IEEE Access*, vol. 8, pp. 50244–50255, 2020.
- [47] X. Gao, L. Dai, J. Zhang, S. Han, and I. Chih-Lin, "Capacity-approaching linear precoding with low-complexity for large-scale MIMO systems," in *2015 IEEE ICC*, 2015, pp. 1577–1582.
- [48] C. Zhang, Y. Jing, Y. Huang, and L. Yang, "Performance analysis for massive MIMO downlink with low complexity approximate zero-forcing precoding," *IEEE Trans. Commun.*, vol. 66, no. 9, pp. 3848–3864, Sept. 2018.
- [49] M. Wu, B. Yin, A. Vosoughi, C. Studer, J. R. Cavallaro, and C. Dick, "Approximate matrix inversion for high-throughput data detection in the large-scale MIMO uplink," in *2013 IEEE ISCAS*, 2013, pp. 2155–2158.
- [50] H. Prabhju, J. Rodrigues, O. Edfors, and F. Rusek, "Approximative matrix inverse computations for very-large mimo and applications to linear precoding systems," in *2013 IEEE WCNC*, 2013, pp. 2710–2715.
- [51] C. Lee, C.B. Chae, T. Kim, S. Choi, and J. Lee, "Network massive MIMO for cell-boundary users: From a precoding normalization perspective," in *2012 IEEE Globecom Workshops*, 2012, pp. 233–237.
- [52] K. Wong and Z. Pan, "Array gain and diversity order of multiuser MISO antenna systems," *Int. J. Wirel. Inf. Netw.*, vol. 15, no. 2, pp. 82–89, Jun. 2008.
- [53] D. Zhu, B. Li, and P. Liang, "On the matrix inversion approximation based on neumann series in massive MIMO systems," in *2015 IEEE ICC*, 2015, pp. 1763–1769.
- [54] L. Hanlen and A. Grant, "Capacity analysis of correlated MIMO channels," *IEEE Trans. Inf. Theory*, vol. 58, no. 11, pp. 6773–6787, Nov. 2012.